High-dose-rate brachytherapy as monotherapy for prostate cancer: technique, rationale and perspective

Yasuo Yoshioka, MD, PhD[1], Osamu Suzuki, MD, PhD[1], Yuki Otani, PhD[1], Ken Yoshida, MD, PhD[2], Takayuki Nose, MD, PhD[3], Kazuhiko Ogawa, MD, PhD[1]

[1]Department of Radiation Oncology, Osaka University Graduate School of Medicine, Osaka, Japan; [2]Department of Radiology, Osaka Medical College, Osaka, Japan, [3]Department of Radiation Oncology, Nippon Medical School Tama Nagayama Hospital, Tokyo, Japan

Abstract

High-dose-rate (HDR) brachytherapy as monotherapy is a comparatively new brachytherapy procedure for prostate cancer. Although clinical results are not yet mature enough, it is a highly promising approach in terms of potential benefits for both radiation physics and radiobiology. In this article, we describe our technique for monotherapeutic HDR prostate brachytherapy, as well as the rationale and theoretical background, with educational intent.

J Contemp Brachytherapy 2014; 6, 1: 91-98

DOI: 10.5114/jcb.2014.42026

Purpose

Multiple treatment options are available for clinically localized prostate cancer, including radical prostatectomy, external beam radiotherapy (EBRT), brachytherapy, and a combination of EBRT and brachytherapy. Brachytherapy in the form of a permanent low-dose-rate (LDR) seed implant, or as high-dose-rate (HDR) afterloading, can deliver a highly localized radiation dose to the tumor. While LDR brachytherapy has been examined and assessed the most, and become a standard treatment option, HDR brachytherapy has recently gained momentum as an alternative. Several features of HDR brachytherapy, including uniformly accurate, precise, and reproducible dosimetry resulting from its advanced optimization capabilities, radiobiological and radioprotective advantages, as well as reduced costs, have made HDR attractive for the treatment of prostate cancer. These advantages avoid the dosimetric uncertainties of LDR related to post implant volume changes, due to needle trauma and subsequent edema during the overall treatment period of several months. High-dose-rate significantly improves the radiation dose distribution, because it can modulate and accurately control both the spatial source position and dwell time during treatment [1].

Historically, HDR brachytherapy was introduced to boost EBRT [2,3]. However, this combination typically adds 4-5 weeks to the time needed for completion of EBRT, in addition to hospitalization for HDR brachytherapy [4].

High-dose-rate brachytherapy as monotherapy, on the other hand, would definitely be the most efficient method of achieving a high degree of conformity and dose escalation. Our group was the first to report on the use of HDR brachytherapy as monotherapy [5], and subsequently reported its promising preliminary and interim outcomes [6-9]. However, to date there are only a small number of centers worldwide that carry out HDR monotherapy. Because HDR monotherapy does not include supplemental EBRT, it requires technical maturity in terms of both implant technique and treatment planning. A special patient care protocol is also needed to manage the single implant over several days of treatment. The aim of this article is to describe our technique and rationale for prostate HDR monotherapy, and to put it in perspective, with educational intent.

Guidelines and recommendations on high-dose-rate brachytherapy for prostate cancer

Clinical results for EBRT and HDR brachytherapy combination therapy have been accumulating, and they culminated in recommendations by the Groupe Européen de Curiethérapie/European Society for Radiotherapy and Oncology (GEC-ESTRO) [10,11], and consensus guidelines by the American Brachytherapy Society (ABS) [12]. The updated National Comprehensive Cancer Network (NCCN) guidelines in the USA state that HDR brachytherapy can be used in combination with EBRT (40-50 Gy) instead of

LDR [13]. As yet, however, no guidelines or recommendations have been established on HDR monotherapy for prostate cancer, therefore it should be undertaken in clinical trial settings.

Suitable patients for high-dose-rate monotherapy

Patient selection criteria for HDR prostate monotherapy are the subject of hot debate. Although our group's initial indication for HDR monotherapy was low- to high-risk prostate cancer [5], subsequent researchers limited indications to low-risk or low-to-intermediate-risk patients [14-17]. As a result, some investigators maintained that HDR monotherapy was suitable only for low-risk or low-to-intermediate risk patients, and a combination of EBRT and HDR brachytherapy for intermediate- to high-risk patients, thus emulating the scheme for LDR brachytherapy. However, recently published reports with a relatively large number of patients revealed excellent biochemical control rates, even for intermediate- and high-risk patients [18-20], including our reports [8,9]. Moreover, considering HDR monotherapy's capability to irradiate even extracapsular lesions, we think there is no reason to limit its indications to low-risk patients, and such indications now tend to be extended to high-risk patients. Our eligibility criteria are: 1) stage T1c-T3b, or T4 with only bladder neck invasion and N0M0 as established by clinical, biochemical, and imaging studies, including magnetic resonance imaging, computed tomography (CT), and bone scans; 2) suitable candidate for epidural anesthesia; and 3) informed consent. Patients are eligible for treatment independent of gland size, provided there is a sufficiently broad pelvic inlet and freedom from lower urinary tract symptoms. Patients are considered ineligible when they have had previous pelvic radiotherapy, surgery or transurethral resection of the prostate. Characteristics of our patients (who were accrued consecutively in the clinical trial setting and for whom informed consents were obtained) are shown in Table 1, with information on accompanying hormone therapy.

Details of technique

Applicator needle implant (Fig. 1A-C)

The implant technique has been previously described in detail by our group [5]. Under epidural anesthesia, the patient is placed in a dorsal lithotomy position, with the perineal region sterilized. A balloon catheter is inserted into the bladder, with air-mixed gel placed within the prostatic urethra to enable visualization of the urethra on ultrasonography (US). Under real-time transrectal-US (TRUS) guidance, metallic applicator needles (Trocar Point Needles and Needle Stoppers®; Nucletron, an Elekta company, Sweden) are placed through the perineal skin, using our in-house template. The template is made of transparent acryl with 167 needle holes spaced at 5 mm intervals. The needles are placed along the line that encompasses the prostate at the largest cross-section on US, except for the rectal side where the needles are placed 2-3 mm inside the prostate contour. For T3 tumors, needles can be placed

outside the prostate capsule and/or into the seminal vesicles. Inner needles are inserted at 1-cm intervals, to adequately cover the base and apex of the prostate, taking care in avoiding the urethra. The total number of needles inserted is usually around 15. The tips of the needles are placed 2 cm within the bladder pouch for the reason described in the following section. We recommend placing three or four metallic fiducial markers inside the prostate gland, as far apart as possible, with at least one at the base and another at the apex. They are useful for recognizing the relative shift between the prostate and the needles, as well as deformation of the prostate itself due to edema.

Treatment planning (Fig. 2A, B)

After the implantation of the needles, CT data are acquired with the patient in the supine position (not in lithotomy). The CT slice thickness is 1.25 mm in helical mode. One hour before CT data acquisition and each irradiation fraction, the urinary balloon catheter is clamped in place to keep the urine within the bladder pouch, so that the cranial side of the bladder wall and the bowel are kept away from the irradiation volume.

Computed tomography-based treatment planning is performed with the aid of Oncentra® Brachy (Nucletron, an Elekta company, Sweden). The clinical target volume (CTV) includes the whole prostate gland with a 5-mm margin, except for the posterior (rectal) margin, which varies from 2 to 5 mm depending on the distance to the rectal wall. If extracapsular and/or seminal vesicle invasion are observed or strongly suspected, that area is included in the CTV and applicators are placed there. The planning target volume (PTV) is equal to the CTV, except in the cranial direction where it is increased by 1 cm, and includes the bladder base. The top 2 cm of the applicators are placed within the bladder pouch, so that the PTV includes a 1 cm margin in the cranial direction around the CTV. This margin is established, not only to avoid the cold area at the base of the prostate, but also to compensate for possible needle displacement in the caudal direction.

The dose distribution is created by geometric optimization (volume method) and manual modification. The following dose constraints are applied: the dose to the whole urethra should be 100-150% of the prescription dose, preferably < 125%, and the dose to the whole rectal mucosa should be < 100% of the prescription dose, preferably < 80%. The PTV coverage requirements are $D_{90} > 100\%$ (mandatory) and $V_{100} > 97\%$ (preferable). The dose-volume constraint for the rectum is $D_{5cc} < 55\%$, which is drawn from our previous analysis, where $D_{5cc} < 27$ Gy is a significant cut-off value for late rectal toxicity [21]. The biologically effective dose (BED) of 27 Gy in 9 fractions in the previous analysis corresponded to 55% of the prescription dose in our ongoing dose-fractionation of 45.5 Gy in 7 fractions, assuming an α/β value for rectal mucosa of 3 Gy.

Patient management

The patient remains in bed for 4 days from Monday (implant day: Day 1) to Thursday (removal day: Day 4)
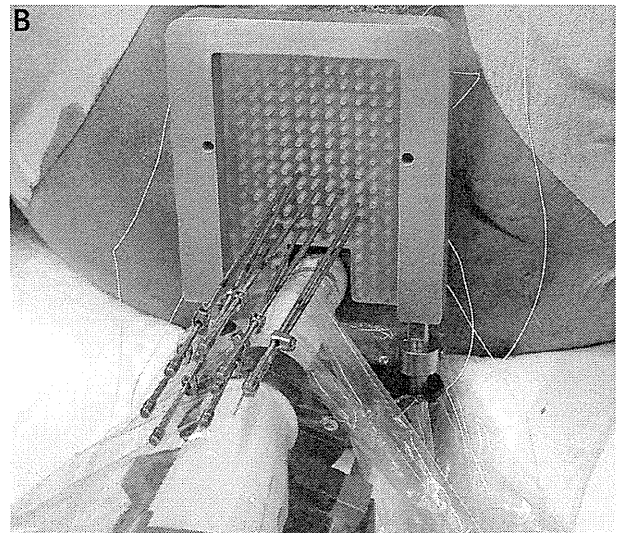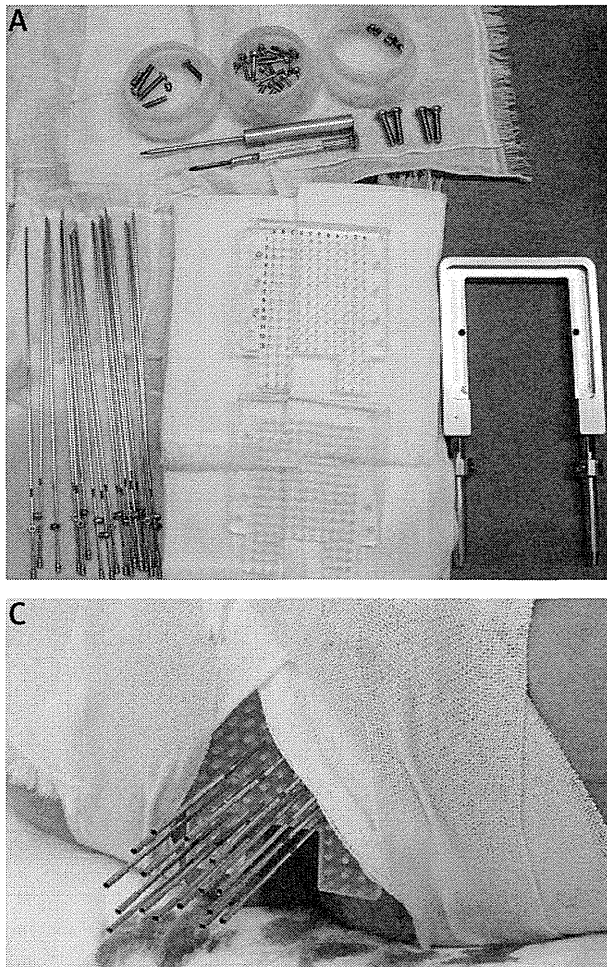
Fig. 1. A) Preparation for implant of applicator needles for HDR prostate brachytherapy. An in-house "see-through" template and its cover plate (center), an in-house metallic frame to hold and connect the template with an ultrasonography-probe stepper (right), applicator needles with stoppers (left), and their screws and screw drivers (upper). B) Needle implant under real-time transrectal-ultrasonography guidance. The patient is awake, under epidural anesthesia, in lithotomy position. Template holes had been superimposed on the ultrasonography monitor. C) Fixation of the template with elastic tape. Before taping, the template had been sutured to the perineal skin. Needle stoppers are sandwiched by the template and its cover plate, preventing needle displacement
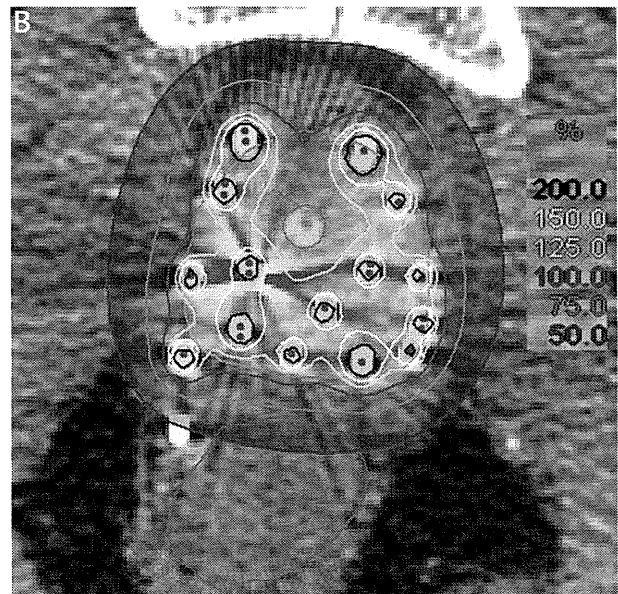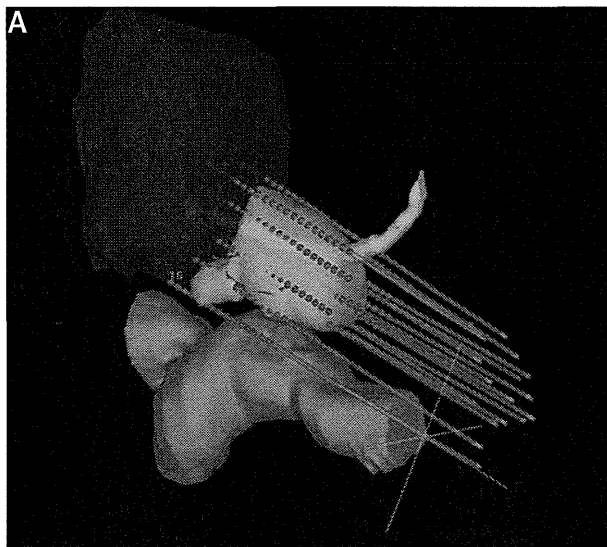

Fig. 2. A) Three-dimensional reconstruction of the prostate and proximal seminal vesicles (pink), rectum (green), bladder (blue), urethra (cyan), and applicator needles and source dwell positions (red). Dwell positions were automatically selected by designating the area up to 7-mm outside the prostate or seminal vesicles. Note that some needles and dwell positions were entirely outside the prostate grand and/or partly in the seminal vesicles or in the bladder pouch. B) A dose distribution plot of transverse plane. Note that the urethral dose was < 125% of the prescription dose, and the rectal dose < 75%. Most parts of the rectum received < 50% of the prescription dose, which would be difficult to achieve with EBRT (even with IMRT)

Table 1. Patient characteristics at Osaka University Hospital

Years	1995-1996	1996-2005	2005-2010*
Dose-fractionation	48 Gy/8 fr/5 days	54 Gy/9 fr/5 days	45.5 Gy/7 fr/4 days
Number of patients	7	112	63
Age median (range)	67 (45-78)	68 (47-81)	69 (50-82)
T classification:			
T1	0	28	15
T2	1	34	32
T3	4	46	14
T4	2	4	2
Gleason score:			
≤ 6	1	50	11
7	1	36	34
≥ 8	0	26	18
Pretreatment PSA (ng/ml):			
< 10.0	1	31	26
10.0-20.0	0	31	22
≥ 20.0	6	50	15
Median (range)	36.3 (7.0-150.0)	16.6 (3.8-233.0)	11.5 (3.9-378.5)
Risk group**:			
Low	0	15	–***
Intermediate	1	29	34
High	6	68	29
Hormone therapy			
Low	–	9 (60%)	–
Median duration (range) (mo)	–	16 (5-36)	–
Intermediate	0 (0%)	19 (66%)	12 (35%)
Median duration (range) (mo)	–	12 (3-156)	7 (1-24)
High	5 (83%)	66 (97%)	25 (86%)
Median duration (range) (mo)	54 (45-180)	43 (2-188)	24 (4-94)
Follow-up (years)			
Median (range)	6.8 (3.3-17.4)	5.4 (1.3-11.4)	3.5 (1.1-6.0)

fr – fractions, PSA – prostate-specific antigen, mo – months
*Only patients until 2010 are reported, but this regimen is still ongoing. **Low (T1c-2a, GS ≤ 6 and PSA < 10), intermediate (T2b-2c, GS – 7 or PSA 10-20), high (T3-4, GS ≥ 8 or PSA ≥ 20). ***I-125 seed permanent implant is indicated from 2005

under continuous epidural anesthesia, and undergoes irradiation twice daily with an interval of ≥ 6 hours. The treatment consists of 7 fractions of 6.5 Gy each (total 45.5 Gy). Anticoagulated patients are told to stop their drugs 1-2 weeks before the implant. To suppress defecation, the patients are given low-residue meals from Day 1 to Day 4. The patients should be given purgatives starting 4 days before the implant (magnesium oxide for 3 days and sennoside the night before) and a glycerin enema early in the morning of Day 1. The patients should also be encouraged to defecate before the implant. Prophylactic antibiotics are administered intravenously on Day 1 and Day 4, at the time of needle insertion and removal, and orally 3 times daily on Day 2 and Day 3. Pneumatic compression devices are attached to the patients' lower legs to prevent deep vein thrombosis from Day 1 through Day 4. To minimize bleeding (both from the perineum and intravesically), a coagulating agent (carbazochrome) is ad-

ministered through an intravenous drip at the time of the implant and at the time of needle removal. Immediately after pulling the needles out, the physician should manually compress the prostate using both hands, one via the perineum and the other via the rectum (as in a digital examination), to stop the bleeding. In addition, pulling the balloon catheter, which has been replaced with a larger 3-way catheter for bladder irrigation, with the balloon inflated to its maximum, helps to stop bleeding from the bladder neck. For intravesical bleeding, bladder irrigation with cold saline is effective, and the continuous bladder irrigation technique is used to prevent clots from occluding the balloon catheter when intravesical bleeding is protracted.

Neoadjuvant and/or adjuvant hormone therapy

The benefits of neoadjuvant and/or adjuvant hormone therapy are controversial. We assume that the therapy's

Table 2. Clinical results of HDR brachytherapy as monotherapy for prostate cancer

Author [ref.]	HDR physical dose			BED (Gy)		EQD$_{2Gy}$ (Gy)		No. of patients	Median follow-up (y)	Biochemical control (risk group)	Late toxicity ≥ Grade 2*	
	Dose/ fraction	Fractions (no. of implants)	Total dose	α/β = 1.5 Gy	α/β = 3.0 Gy	α/β = 1.5 Gy	α/β = 3.0 Gy				GU	GI
Yoshioka [9]	6 Gy	8 (1 implant)	48 Gy	240	144	103	86	7	NA	NA	NA	NA
	6 Gy	9 (1 implant)	54 Gy	270	162	116	97	112	5.4	85% low-risk at 5 y 93% intermediate-risk at 5 y 79% high-risk at 5 y	7.1%	7.1%
	6.5 Gy	7 (1 implant)	45.5 Gy	243	144	104	86	63	3.5	96% intermediate-risk at 3 y 90% high-risk at 3 y	6.3%	1.6%
Demanes [15]	7 Gy	6 (2 implant)	42 Gy	238	140	102	84	298	5.2	97% low- and intermediate-risk at 5 y	28.9%	< 1.0%
Martinez [24]	9.5 Gy	4 (1 implant)	38 Gy	279	158	119	95	248	4.8	88% low- and intermediate-risk at 5 y	40.5%	2.0%
Ghilezan [17]	12 Gy	2 (1 implant)	24 Gy	216	120	93	72	50	1.4	NA	25.5%	5.3%
	13.5 Gy	2 (1 implant)	27 Gy	270	149	116	89	44				
Rogers [18]	6.5 Gy	6 (2 implant)	39 Gy	208	124	89	74	284	2.7	94% intermediate-risk at 5 y	7.7%	0.0%
Zamboglou [20]	9.5 Gy	4 (1 implant)	38 Gy	279	158	119	95	141	4.4	95% low-risk at 5 y 93% intermediate-risk at 5 y 93% high-risk at 5 y	27.5%	2.6%
	9.5 Gy	4 (2 implant)	38 Gy	279	158	119	95	351				
	11.5 Gy	3 (3 implant)	34.5 Gy	299	167	128	100	226				
Hoskin [19]	8.5 Gy	4 (1 implant)	34 Gy	227	130	97	78	30	4.5	99% intermediate-risk at 3 y 91% high-risk at 3 y	33.0%	13.0%
	9 Gy	4 (1 implant)	36 Gy	252	144	108	86	25	5.0		40.0%	4.0%
	10.5 Gy	3 (1 implant)	31.5 Gy	252	142	108	85	109	2.8		34.0%	7.0%
Hoskin [22]	13 Gy	2 (1 implant)	26 Gy	251	139	108	83	115	0.2	NA	5%	1%
	19 Gy	1 (1 implant)	19 Gy	260	139	111	84	24	0.2		0%	0%
	20 Gy	1 (1 implant)	20 Gy	287	153	123	92	26	0.2		9%	5%
Ghadjar [27]	9.5 Gy	4 (1 implant)	38 Gy	279	158	119	95	36	3.0	100% low- and intermediate-risk at 3 y	36.1%	5.6%
Barkati [16]	10 Gy	3 (1 implant)	30 Gy	230	130	99	78	19	3.3	88% low- and intermediate-risk at 3 y	59.0%	5.1%
	10.5 Gy	3 (1 implant)	31.5 Gy	252	142	108	85	19				
	11 Gy	3 (1 implant)	33 Gy	275	154	118	92	19				
	11.5 Gy	3 (1 implant)	34.5 Gy	299	167	128	100	22				
Prada [23]	19 Gy	1 (1 implant)	19 Gy	260	139	111	84	40	1.6	100% low-risk at 2.7 y 88% intermediate-risk at 2.7 y	0.0%	0.0%

HDR – high-dose-rate; BED – biologically effective dose; EQD$_{2Gy}$ – biologically equivalent dose in 2-Gy fractions; GU – genitourinary; GI – gastrointestinal; NA – not applicable

Scored per event not per patient

additional benefit over RT alone would be smaller in the case of HDR brachytherapy than for EBRT (for example, classical 70-Gy EBRT), because BED of HDR brachytherapy is far higher than that of EBRT. However, some interaction between hormones and radiation may still occur, and the volume reduction effect may be associated with less toxicity. In our present protocol, patients with only one intermediate-risk feature are not given hormone therapy. The other intermediate-risk and all high-risk patients receive 6 to 12 months of neoadjuvant hormone therapy, but no adjuvant. If high-risk patients prefer to have long-term hormone therapy after being informed of its survival benefit in the case of EBRT, then adjuvant hormone therapy is allowed for up to 3 years total duration.

Patient outcomes

Table 2 lists clinical results of monotherapeutic HDR brachytherapy for prostate from the literature [5-7,15-20, 22-27]. Only 10 institutions worldwide have reported clinical results for prostate HDR monotherapy. The longest median follow-up was 5.4 years, which was reported from our institution [8], while the median follow-up of most of the studies was only 1-3 years.

The reported 5-year prostate-specific antigen (PSA) control rate for low-risk groups ranged from 85-97%, mostly > 90%. For intermediate-risk groups, some authors reported a PSA control rate of 93-94%, and for high-risk groups, it was reported between 79 and 93%, mostly > 80%. Although none of these studies have reported a follow-up period much beyond 5 years, the overall PSA control rates reported thus far have been excellent, which may be attributed to the high BED of > 200 Gy discussed

Fig. 3. Treatment planning CT on the implant day (magenta) and on the last irradiation day (Day 4, gray), which were overlaid by matching positions of the metallic fiducial marker (VISICOIL®). Note that the geometry of needle fiducial template was kept constant, in contrary to the shift of pubic symphysis or sacral bone. However, the needles moved about 1 cm in the caudal direction, together with the template, which might be attributable to the perineal edema

in the following section. The reported toxicity levels were generally acceptable (Table 2).

Advantages/disadvantages of high-dose-rate monotherapy

Advantages and disadvantages of prostate HDR monotherapy, compared to other treatment options, have been detailed in our review article published elsewhere [28]. Below are the summaries, including (1-4) description of advantages with respect to radiation physics, (5) advantages with respect to radiobiology, and (6) disadvantages:

1. Medical staff are never exposed to radiation and patients can stay in a regular ward since there is no need for a shielded room. Patients only need to go to an HDR unit room for irradiation for 30 minutes per fraction.
2. Treatment planning is based on the CT images obtained after needle insertion, or on the TRUS images obtained at the time of needle insertion. The dwell positions of the stepping source are determined in terms of real anatomy. The dwell time for each dwell position is then calculated with an optimization algorithm.
3. Unlike for EBRT, inter-/intra-fraction organ motion is not a problem with HDR brachytherapy. In the case of EBRT, several factors including daily set-up errors, retention of feces, gas, or urine, respiratory motion, or peristaltic motion result in discrepancies between the coordinates of the tumor and the radiation beam. With brachytherapy, these two coordinates are always concordant, because the tumor and the radioactive sources move in unison, so that PTV is normally identical to CTV. The overall treatment time for HDR monotherapy typically ranges from 1-4 days, significantly shorter than for EBRT.
4. Unlike for LDR brachytherapy, HDR brachytherapy needles can be placed at the extracapsular lesion, and even into the seminal vesicles and/or into the bladder pouch. The cable-connected stepping source simply moves back and forth within the closed space without any risk of source migration or dropping out. Therefore, the indication for HDR monotherapy can potentially even be extended to T3a/b or some T4 tumors. The dwell time optimization makes a significant urethral dose reduction possible for HDR compared to that for LDR.
5. Recent findings that the α/β value for prostate cancer is less than that for the surrounding late-responding normal tissue have made hypofractionation attractive, and HDR monotherapy can maximize this advantage of hypofractionation [29-33]. Table 2 lists dose-fractionations and associated BED and EQD_{2Gy} of HDR monotherapy from the literature. The BED for prostate cancer ranges from 208-299 Gy, with a median of 256 Gy. The values for EQD_{2Gy} range from 89-128 Gy with a median of 110 Gy, which may be impossible to administer with EBRT, even with IMRT. As for late toxicity, EQD_{2Gy} ranges from 72-110 Gy, with a median of 86 Gy, which can be considered the equivalent of the maximum dose of 86.4 Gy administered with the current IMRT. This means that, theoretically, hypofrac-

tionation with a large fraction size can enhance BED for prostate cancer without increasing BED for late-responding tissue.

6. One of the possible drawbacks of HDR brachytherapy is the problem of applicator needle displacement during treatment (Fig. 3), which has been pointed out by some groups [14,34-41]. However, this problem does not arise if there is one fraction per implant [20-23]. Another drawback of HDR is the requirement of hospitalization and patients having to stay in bed during the treatment period. Further potential disadvantages of HDR are tumor edema and bleeding from needle insertion, causing changes in dosimetry from planning to treatment. In addition, if large doses are given to normal tissues (perhaps in less experienced centers), there is an increased risk of late toxicity, given the large dose per fraction.

Future directions

High-dose-rate prostate monotherapy is still evolving and being developed, with ongoing research to determine optimal methodology and dose-fractionations. At our affiliated hospital, a new technique enabling more accurate implantation into seminal vesicles, and a new ambulatory technique for multi-fraction HDR brachytherapy have been developed [42,43]. In view of its high degree of freedom, there may still be some room for improvement in the dwell time optimization algorithm [44,45]. As for the problem of needle displacement, we are now testing daily CT scans to adjust needle positions or source dwell positions, by means of readjusting the relative locations of dwell positions to the gravity of the implanted fiducial markers. However, this method causes additional radiation exposure to the patient, which should be taken in to account as an intrinsic disadvantage.

Recent trends are moving towards a smaller number of fractions and shorter treatment. Many institutions previously used 4 fractions or more [5,14,15,18]. However, researchers recently reported 3 fractions with 3 implants (1 fraction per implant) [20], 2 fractions in a single day [17], and even single fraction HDR monotherapy [22,23]. Such an extremely hypofractionated regimen would maximize the therapeutic ratio, and at the same time avoid the HDR brachytherapy drawbacks of hospitalization and needle displacement during the treatment period. Finally, the authors would like to emphasize that HDR monotherapy has the largest potential to control prostate cancer without compromising toxicity, from the perspective of both radiation physics and radiobiology. Further clinical research is therefore clearly warranted.

Disclosure

Authors report no conflict of interest.

References

1. Skowronek J. Low-dose-rate or high-dose-rate brachytherapy in treatment of prostate cancer – between options. J Contemp Brachytherapy 2013; 5: 33-41.
2. Galalae RM, Kovács G, Schultze J et al. Long-term outcome after elective irradiation of the pelvic lymphatics and local dose escalation using high-dose-rate brachytherapy for locally advanced prostate cancer. Int J Radiat Oncol Biol Phys 2002; 52: 81-90.
3. Mate TP, Gottesman JE, Hatton J et al. High dose-rate afterloading Ir-192 prostate brachytherapy: feasibility report. Int J Radiat Oncol Biol Phys 1998; 41: 525-533.
4. Hijazi H, Chevallier D, Gal J et al. Prostate cancer boost using high-dose rate brachytherapy: early toxicity analysis of 3 different fractionation schemes. J Contemp Brachytherapy 2013; 5: 203-209.
5. Yoshioka Y, Nose T, Yoshida K et al. High-dose-rate interstitial brachytherapy as a monotherapy for localized prostate cancer: treatment description and preliminary results of a phase I/II clinical trial. Int J Radiat Oncol Biol Phys 2000; 48: 675-681.
6. Yoshioka Y, Nose T, Yoshida K et al. High-dose-rate brachytherapy as monotherapy for localized prostate cancer: a retrospective analysis with special focus on tolerance and chronic toxicity. Int J Radiat Oncol Biol Phys 2003; 56: 213-220.
7. Yoshioka Y, Konishi K, Oh RJ et al. High-dose-rate brachytherapy without external beam irradiation for locally advanced prostate cancer. Radiother Oncol 2006; 80: 62-68.
8. Yoshioka Y, Konishi K, Sumida I et al. Monotherapeutic high-dose-rate brachytherapy for prostate cancer: Five-year results of an extreme hypofractionation regimen with 54 Gy in nine fractions. Int J Radiat Oncol Biol Phys 2011; 80: 469-475.
9. Yoshioka Y, Konishi K, Suzuki O et al. Monotherapeutic high-dose-rate brachytherapy for prostate cancer: a dose reduction trial. Radiother Oncol 2014; 110: 114-119.
10. Kovács G, Pötter R, Loch T et al. GEC/ESTRO-EAU recommendations on temporary brachytherapy using stepping sources for localised prostate cancer. Radiother Oncol 2005; 74: 137-148.
11. Hoskin PJ, Colombo A, Henry A et al. GEC/ESTRO recommendations on high dose rate afterloading brachytherapy for localised prostate cancer: an update. Radiother Oncol 2013; 107: 325-332.
12. Yamada Y, Rogers L, Demanes DJ et al; American Brachytherapy Society. American Brachytherapy Society consensus guidelines for high-dose-rate prostate brachytherapy. Brachytherapy 2012; 11: 20-32.
13. National Comprehensive Cancer Network (NCCN) Clinical Practice Guidelines in Oncology. Prostate Cancer. Version 4. 2013. http://www.nccn.org/professionals/physician_gls/pdf/prostate.pdf; accessed: Nov. 20, 2013.
14. Martinez A, Pataki I, Edmundson G et al. Phase II prospective study of the use of conformal high-dose-rate brachytherapy as monotherapy for the treatment of favorable stage prostate cancer: a feasibility report. Int J Radiat Oncol Biol Phys 2001; 49: 61-69.
15. Demanes DJ, Martinez AA, Ghilezan M et al. High-dose-rate monotherapy: safe and effective brachytherapy for patients with localized prostate cancer. Int J Radiat Oncol Biol Phys 2011; 81: 1286-1292.
16. Barkati M, Williams SG, Foroudi F et al. High-dose-rate brachytherapy as a monotherapy for favorable-risk prostate cancer: a phase II trial. Int J Radiat Oncol Biol Phys 2012; 82: 1889-1896.
17. Ghilezan M, Martinez A, Gustason G et al. High-dose-rate brachytherapy as monotherapy delivered in two fractions within one day for favorable/intermediate-risk prostate cancer: preliminary toxicity data. Int J Radiat Oncol Biol Phys 2012; 83: 927-932.
18. Rogers CL, Alder SC, Rogers RL et al. High dose brachytherapy as monotherapy for intermediate risk prostate cancer. J Urol 2012; 187: 109-116.

19. Hoskin P, Rojas A, Lowe G et al. High-dose-rate brachytherapy alone for localized prostate cancer in patients at moderate or high risk of biochemical recurrence. *Int J Radiat Oncol Biol Phys* 2012; 82: 1376-1384.

20. Zamboglou N, Tselis N, Baltas D et al. High-dose-rate interstitial brachytherapy as monotherapy for clinically localized prostate cancer: treatment evolution and mature results. *Int J Radiat Oncol Biol Phys* 2013; 85: 672-678.

21. Konishi K, Yoshioka Y, Isohashi F et al. Correlation between dosimetric parameters and late rectal and urinary toxicities in patients treated with high-dose-rate brachytherapy used as monotherapy for prostate cancer. *Int J Radiat Oncol Biol Phys* 2009; 75: 1003-1007.

22. Hoskin P, Rojas A, Ostler P et al. High-dose-rate brachytherapy alone given as two or one fraction to patients for locally advanced prostate cancer: acute toxicity. *Radiother Oncol* 2014; 110: 268-271.

23. Prada PJ, Jimenez I, González-Suárez H et al. High-dose-rate interstitial brachytherapy as monotherapy in one fraction and transperineal hyaluronic acid injection into the perirectal fat for the treatment of favorable stage prostate cancer: treatment description and preliminary results. *Brachytherapy* 2012; 11: 105-110.

24. Martinez AA, Demanes J, Vargas C et al. High dose rate prostate brachytherapy: an excellent accelerated hypofractionated treatment for favorable prostate cancer. *Am J Clin Oncol* 2010; 33: 481-488.

25. Martin T, Baltas D, Kureck R et al. 3D conformal HDR brachytherapy as monotherapy for localized prostate cancer. A pilot study. *Strahlenther Oncol* 2004; 180: 225-232.

26. Corner C, Rajas AM, Bryant L et al. A Phase II study of high dose rate afterloading brachytherapy as monotherapy for the treatment of localized prostate cancer. *Int J Radiat Oncol Biol Phys* 2008; 72: 441-446.

27. Ghadjar P, Keller T, Pentsch CA et al. Toxicity and early treatment outcomes in low and intermediate-risk prostate cancer managed by high-dose rate brachytherapy as monotherapy. *Brachytherapy* 2009; 8: 45-51.

28. Yoshioka Y, Yoshida K, Yamazaki H et al. The emerging role of high-dose-rate (HDR) brachytherapy as monotherapy for prostate cancer. *J Radiat Res* 2013; 54: 781-788.

29. Brenner DJ, Hall EJ. Fractionation and protraction for radiotherapy of prostate carcinoma. *Int J Radiat Oncol Biol Phys* 1999; 43: 1095-1101.

30. Fowler J, Chappell R, Ritter M. Is alpha/beta for prostate tumors really low? *Int J Radiat Oncol Biol Phys* 2001; 50: 1021-1031.

31. Brenner DJ, Martinez AA, Edmundson GK et al. Direct evidence that prostate tumors show high sensitivity to fractionation (low alpha/beta ratio), similar to late-responding normal tissue. *Int J Radiat Oncol Biol Phys* 2002; 52: 6-13.

32. Wang JZ, Guerrero M, Li XA. How low is the alpha/beta ratio for prostate cancer? *Int J Radiat Oncol Biol Phys* 2003; 55: 194-203.

33. Miralbell R, Roberts SA, Zubizarreta E et al. Dose-fractionation sensitivity of prostate cancer deduced from radiotherapy outcomes of 5,969 patients in seven international institutional datasets: $\alpha/\beta = 1.4$ (0.9-2.2) Gy. *Int J Radiat Oncol Biol Phys* 2012; 82: e17-24.

34. Damore SJ, Syed AM, Puthawala AA et al. Needle displacement during HDR brachytherapy in the treatment of prostate cancer. *Int J Radiat Oncol Biol Phys* 2000; 46: 1205-1211.

35. Hoskin PJ, Bownes PJ, Ostler P et al. High dose rate afterloading brachytherapy for prostate cancer: Catheter and gland movement between fractions. *Radiother Oncol* 2003; 68: 285-288.

36. Mullokandov E, Gejerman G. Analysis of serial CT scans to assess template and catheter movement in prostate HDR brachytherapy. *Int J Radiat Oncol Biol Phys* 2004; 58: 1063-1071.

37. Simnor T, Li S, Lowe G et al. Justification for inter-fraction correction of catheter movement in fractionated high dose-rate brachytherapy treatment of prostate cancer. *Radiother Oncol* 2009; 93: 253-258.

38. Yoshida K, Yamazaki H, Nose T et al. Needle applicator displacement during high-dose-rate interstitial brachytherapy for prostate cancer. *Brachytherapy* 2010; 9: 36-41.

39. Foster W, Cunha JA, Hsu IC et al. Dosimetric impact of interfraction catheter movement in high-dose rate prostate brachytherapy. *Int J Radiat Oncol Biol Phys* 2011; 80: 85-90.

40. Kolkman-Deurloo IK, Roos MA, Aluwini S. HDR monotherapy for prostate cancer: A simulation study to determine the effect of catheter displacement on target coverage and normal tissue irradiation. *Radiother Oncol* 2011; 98: 192-197.

41. Takenaka T, Yoshida K, Ueda M et al. Assessment of daily needle applicator displacement during high-dose-rate interstitial brachytherapy for prostate cancer using daily CT examinations. *J Radiat Res* 2012; 53: 469-474.

42. Yoshida K, Nose T, Shiomi H et al. New ambulatory implant technique of high-dose-rate interstitial brachytherapy for prostate cancer. *Radiat Med* 2006; 24: 595-599.

43. Yoshida K, Kuroda S, Yoshida M et al. New implant technique for separation of the seminal vesicle and rectal mucosa for high-dose-rate prostate brachytherapy. *Brachytherapy* 2007; 6: 180-186.

44. Yoshioka Y, Nishimura T, Kamata M et al. Evaluation of anatomy-based dwell position and inverse optimization in high-dose-rate brachytherapy of prostate cancer: a dosimetric comparison to a conventional cylindrical dwell position, geometric optimization, and dose-point optimization. *Radiother Oncol* 2005; 75: 311-317.

45. Sumida I, Shiomi H, Yoshioka Y et al. Optimization of dose distribution for HDR brachytherapy of the prostate using Attraction-Repulsion Model. *Int J Radiat Oncol Biol Phys* 2006; 64: 643-649.
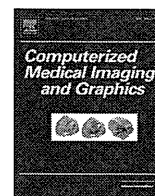
CrossMark

A computerized framework for monitoring four-dimensional dose distributions during stereotactic body radiation therapy using a portal dose image-based 2D/3D registration approach

Takahiro Nakamoto[a], Hidetaka Arimura[b,*], Katsumasa Nakamura[c], Yoshiyuki Shioyama[d],
Asumi Mizoguchi[e], Taka-aki Hirose[f], Hiroshi Honda[c], Yoshiyuki Umezu[f],
Yasuhiko Nakamura[f], Hideki Hirata[b]

[a] Division of Medical Quantum Science, Department of Health Sciences, Graduate School of Medical Sciences, Kyushu University, Fukuoka, Japan
[b] Division of Medical Quantum Science, Department of Health Sciences, Faculty of Medical Sciences, Kyushu University, Fukuoka, Japan
[c] Department of Clinical Radiology, Graduate School of Medical Sciences, Kyushu University, Fukuoka, Japan
[d] Saga Heavy Ion Medical Accelerator in Tosu, Saga, Japan
[e] Kurume University Hospital, Fukuoka, Japan
[f] Kyushu University Hospital, Fukuoka, Japan

ARTICLE INFO

ABSTRACT

A computerized framework for monitoring four-dimensional (4D) dose distributions during stereotactic body radiation therapy based on a portal dose image (PDI)-based 2D/3D registration approach has been proposed in this study. Using the PDI-based registration approach, simulated 4D "treatment" CT images were derived from the deformation of 3D planning CT images so that a 2D planning PDI could be similar to a 2D dynamic clinical PDI at a breathing phase. The planning PDI was calculated by applying a dose calculation algorithm (a pencil beam convolution algorithm) to the geometry of the planning CT image and a virtual water equivalent phantom. The dynamic clinical PDIs were estimated from electronic portal imaging device (EPID) dynamic images including breathing phase data obtained during a treatment. The parameters of the affine transformation matrix were optimized based on an objective function and a gamma pass rate using a Levenberg–Marquardt (LM) algorithm. The proposed framework was applied to the EPID dynamic images of ten lung cancer patients, which included 183 frames (mean: 18.3 per patient). The 4D dose distributions during the treatment time were successfully obtained by applying the dose calculation algorithm to the simulated 4D "treatment" CT images. The mean ± standard deviation (SD) of the percentage errors between the prescribed dose and the estimated dose at an isocenter for all cases was 3.25 ± 4.43%. The maximum error for the ten cases was 14.67% (prescribed dose: 1.50 Gy, estimated dose: 1.72 Gy), and the minimum error was 0.00%. The proposed framework could be feasible for monitoring the 4D dose distribution and dose errors within a patient's body during treatment.

1. Introduction

The aim of radiation therapy is to reduce the dose as low as possible to surrounding normal tissues, while concentrating the dose administered to target tumors. High-precision radiation therapies, such as stereotactic body radiation therapy (SBRT), have been employed to achieve this purpose. SBRT has several unique features, such as the delivery of large doses for small irradiation fields within several fractions (e.g. 48 Gy/4 fractions), and the use of seven to eight beam directions, including coplanar and non-coplanar beam arrangements for localized small tumors in the lung or liver [1]. It has been reported that the treatment outcome of radiation therapy has been similar to or better than that of surgery, depending on type of tumor, stage and location [2–4].

In SBRT, it is substantially necessary to ensure whether the high dose beam is correctly delivered with respect to geometrical and dosimetrical targeting according to the treatment plan. Regarding the geometrical targeting, if tumor location errors, such as patient setup errors, physiological motion, variations of tumors or organs occur at the treatment time, the location errors could result in

* Corresponding author at: Division of Medical Quantum Science, Department of Health Sciences, Faculty of Medical Sciences, Kyushu University, 3-1-1 Maidashi, Higashi-ku, Fukuoka 812-8582, Japan. Tel.: +81 92 642 6719; fax: +81 92 642 6719.
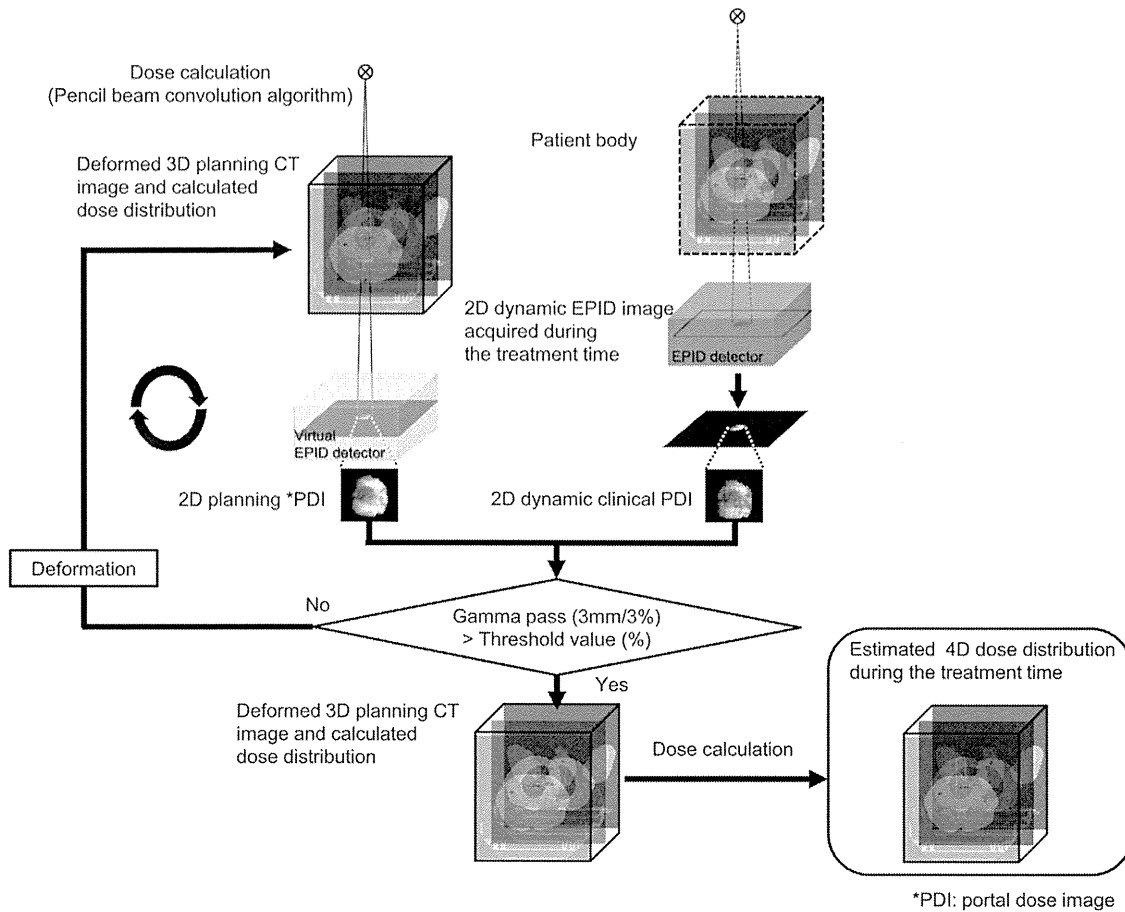E-mail address: arimurah@med.kyushu-u.ac.jp (H. Arimura).

Fig. 1. A conceptual diagram for monitoring 4D dose distributions during the treatment time.

increased normal tissue complication and decreased tumor control [5,6]. Therefore, in SBRT, electronic portal imaging device (EPID) dynamic images are acquired to verify the tumor location within the irradiation field during the treatment dose delivery. However, as for dosimetric targeting, it has not been verified whether the planned dose distribution has been accurately administered to the target during the treatment dose delivery. Therefore, it is essential to monitor four-dimensional (4D) dose distributions for the target and its surrounding normal tissues in the patients' bodies during the treatment time in order to guarantee the quality of the radiation therapy.

A number of methods for estimating the dose distributions in patient bodies or phantoms during the treatment time have been developed [7–11]. The purpose of these methods was to estimate the 3D dose distributions in patient bodies or phantoms to verify the intensity-modulated radiation therapy (IMRT) plans. Several studies on 4D dose distributions obtained using four-dimensional computed tomography (4D-CT), which were affected by respiratory motion, have been reported [12–15]. A common approach of these studies was to apply dose calculation algorithms to breathing phase 4D-CT image sets, which were acquired under the free-breathing condition. These studies were based on the assumption that the breathing phase during the treatment time is very similar to that during 4D-CT scanning.

Gendrin developed a system of monitoring tumor motion by a real-time 2D/3D registration during radiotherapy [16]. The system can monitor three-dimensional tumor movements by registering 3D planning CT images to portal images, which were acquired during the treatment time [16]. In this study, we have proposed a computerized framework for monitoring 4D dose distributions

during the SBRT using a portal dose image (PDI)-based 2D/3D registration approach.

2. Materials and methods

2.1. The overall procedure of the study

Fig. 1 shows a conceptual diagram for monitoring 4D dose distributions during the treatment time. Fig. 2 shows a processing
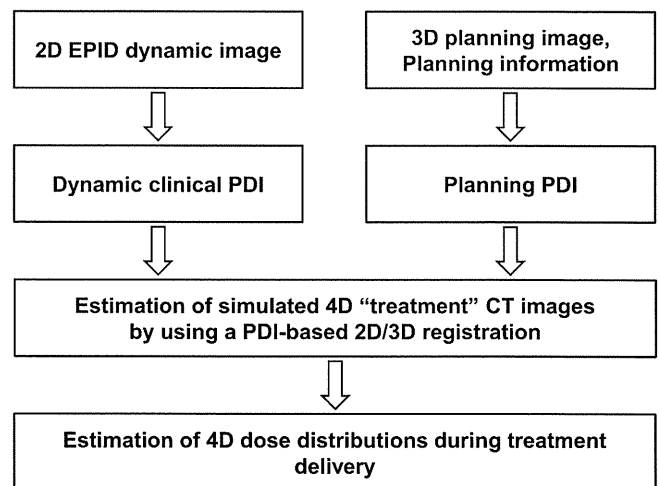

Fig. 2. The processing pipeline for the estimation of the 4D dose distributions using a PDI-based 2D/3D registration approach during treatment delivery.

Table 1
The characteristics of the ten cases evaluated in this study.

Case no.	Age	Gender[a]	Gantry angle (degrees)	No. of frames	Tumor location	Cancer type	Anatomical vicinity	Tumor size (mm) Longitudinal	Width
1	83	F	220	18	Lt. Upper	Unknown	Aorta	27	25
2	51	F	0	21	Rt. Upper	Metastasis	Isolated	20	20
3	83	M	170	20	Lt. Middle	Unknown	Chest wall	30	33
4	56	M	150	20	Rt. Lower	Adenocarcinoma	Diaphragm	15	15
5	75	M	220	18	Lt. Upper	Adenocarcinoma	Aorta	25	20
6	51	F	45	21	Rt. Middle	Adenocarcinoma	Isolated	20	20
7	75	M	270	21	Rt. Upper	Small cell	Mediastinum	38	38
8	72	M	90	19	Lt. Middle	Non-small cell	Chest wall	20	25
9	81	F	180	7	Lt. Middle	Unknown	Chest wall	32	35
10	84	M	150	18	Rt. Middle	Small cell	Chest wall	30	25

[a] F: female, M: male.

pipeline for monitoring 4D dose distributions using the PDI-based 2D/3D registration approach during the treatment delivery. The proposed framework mainly consists of the following four steps. First, a 2D dynamic clinical PDI was derived from the EPID dynamic image based on the deconvolution and convolution of lateral scatter kernels, and a pixel-to-dose conversion function. Second, a 2D planning PDI was obtained by calculating the total energy released per unit mass (TERMA) and applying a dose calculation algorithm for the 3D planning CT image. Third, simulated 4D "treatment" CT images were estimated by deforming 3D planning CT images by using affine transformation matrices so that a 2D planning PDI could be similar to a 2D dynamic clinical PDI at a certain time. The gamma pass rate was used as a similarity index. The parameters of the affine transformation matrices were optimized based on an objective function and a gamma pass rate by a Levenberg–Marquardt (LM) algorithm. Finally, 4D dose distributions during the treatment time were calculated by applying a dose calculation algorithm, i.e., a pencil beam convolution (PBC) algorithm, to simulated 4D "treatment" CT images.

Algorithm 1
An algorithm for the production of the dynamic clinical PDI.

1.	**INPUT** i_E: EPID dynamic image;
2.	k_E: LSK in the EPID;
3.	k_w: LSK of the water equivalent phantom;
4.	**COMMENTS** p_E: incident primary X-ray signal to the EPID;
5.	p_w: incident primary X-ray dose to the water equivalent phantom;
6.	i_w: X-ray dose in the water equivalent phantom;
7.	(Capital symbols indicate spatial frequency domains.)
8.	$I_E \leftarrow$ Fourier transform (i_E), $K_E \leftarrow$ Fourier transform (k_E);
9.	//**Calculation of the incident primary X-ray signal**
10.	$P_E \leftarrow \frac{I_E}{K_E}$;
11.	$p_E \leftarrow$ Inverse Fourier transform (P_E);
12.	//**Conversion of the X-ray signal into the X-ray dose**
13.	$p_w \leftarrow$ Pixel-to-dose conversion function (p_E);
14.	$P_w \leftarrow$ Fourier transform (p_w), $K_w \leftarrow$ Fourier transform (k_w);
15.	//**Calculation of the dynamic clinical PDI**
16.	$I_w \leftarrow P_w \cdot K_w$;
17.	$i_w \leftarrow$ Inverse Fourier transform (I_w);
18.	$I^c \leftarrow i_w$;
19.	**OUTPUT** I^c: dynamic clinical PDI;

2.2. Clinical cases

This study was performed under a protocol approved by the institutional review board of our hospital. Ten patients with lung cancer, who were treated with SBRT from 2004 to 2005, were selected for this study. The patients (six males and four females) had a median age of 75 years (range, 51–84 years). Table 1 shows the characteristics of the ten cases evaluated in this study. All patients received a dose of 48 Gy, prescribed at the isocenter in four fractions, with accelerating voltages of 6 MV on linear accelerators (Clinac 21EX; Varian Medical Systems Inc., Palo Alto, USA). These patients were scanned by using a 4-slice CT scanner (Mx 8000; Philips, Amsterdam, The Netherlands) with 16-bit gray levels, a matrix size of 512 × 512 pixels, and a slice thickness of 2.0 mm. The treatment planning was performed by experienced radiation oncologists on a commercially available radiotherapy treatment planning system (Eclipse version 6.5; Varian Medical System Inc., Palo Alto, USA). The dynamic portal images were acquired on an EPID (Portal Vision aS-500; Varian Medical System Inc., Palo Alto, USA) using 6 MV X-rays with an X-ray converter of amorphous silicon, a phosphor of terbium-activated gadolinium oxysulfide (Gd_2O_2S:Tb), a detection region of 400 × 300 mm^2, a matrix size of 512 × 384 pixels, 16-bit gray levels, and a frame rate of 0.5 frames per second during SBRT. The average and total numbers of frames for the ten cases were 18.3 and 183, respectively. Our proposed framework was implemented in C, and performed by a general purpose personal computer, which was equipped with a 3.30 GHz central processing unit (CPU) (Intel® Core™ i7-3960X CPU) and 32.0 gigabyte (GB) memory.

2.3. Calculation of the dynamic clinical PDI

The dynamic clinical PDI was derived from an EPID dynamic image by applying the deconvolution and convolution of lateral scatter kernels, and a pixel-to-dose conversion function [17]. Fig. 3 shows a conceptual diagram for obtaining a dynamic clinical PDI. Algorithm 1 shows an algorithm for the production of the dynamic clinical PDI.

The lateral scatter kernel (LSK) was considered to be a function, which describes laterally scattered X-rays. In this study, the LSKs of EPID and the water equivalent phantom were calculated by a Monte Carlo simulation [18]. The number of histories was 10^8, which was used for estimation of the both LSKs in the Monte Carlo simulation. The uncertainty of the Monte Carlo simulation was less than 0.5%. In order to estimate the incident primary X-ray signal distributions to the EPID, the EPID dynamic images were deconvolved using the LSK of the EPID.

The incident primary X-ray signal to the EPID was converted into the incident primary X-ray dose to the water equivalent phantom using a pixel-to-dose conversion function.

The pixel-to-dose conversion function was estimated by using the EPID based on Chen's method [17]. The pixel-to-dose conversion function was experimentally measured using the EPID [18]. Errors of EPID dynamic image pixel value and absorbed dose in this measurement were ±0.02% and ±0.09%, respectively. Finally, dynamic clinical PDIs were calculated by convolution of the incident primary X-ray dose to the water equivalent phantom with the LSK of the water equivalent phantom.
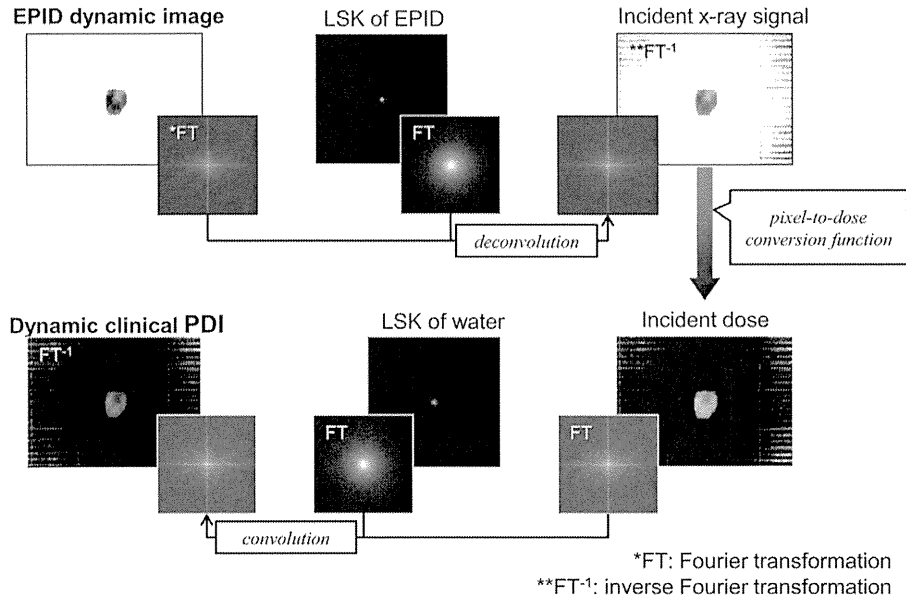
EPID dynamic image   LSK of EPID   Incident x-ray signal

Dynamic clinical PDI   LSK of water   Incident dose

*FT: Fourier transformation
**FT⁻¹: inverse Fourier transformation

Fig. 3. A conceptual diagram for obtaining a dynamic clinical PDI.

2.4. Calculation of the planning PDI

The 2D planning PDI was estimated by calculating the TERMA and applying a dose calculation algorithm in a world coordinate system including a linear accelerator, the 3D planning CT image, and a virtual water phantom. Fig. 4 shows an illustration of a geometry used for the production of the planning PDI from the planning CT images. The source-to-axis distance (SAD) and source-to-image receptor distance (SID) were 100 cm and 140 cm, respectively. The geometric setting was the same as that of the EPID mounted on the linear accelerator. The isocenter in the planning CT image was placed at an SAD of 100 cm. The isocenter coordinate was obtained from a digital imaging and communications in medicine (DICOM) file for radiation therapy, i.e., DICOM-RT. A divergent primary beam with a number of rays produced from the X-ray focal spot of the linear accelerator was virtually delivered to the planning CT image. The X-ray focal spot was estimated based on an actual focal spot size of 1.53 mm [19,20] and a primary collimator angle of 13.9°.

Algorithm 2 shows an algorithm for the production of the planning PDI. The dose distribution was calculated in the planning CT image and the virtual water phantom by using the PBC algorithm [26–28]. The PBC algorithm is expressed by:

$$D(\mathbf{r}) = \int\!\!\int\!\!\int T(\mathbf{r}') \cdot K(\mathbf{r} - \mathbf{r}')d\mathbf{r}' = T(\mathbf{r}) * K(\mathbf{r}), \tag{1}$$

where D is the absorbed dose (Gy), $\mathbf{r}$ is the 3D position vector, T is the TERMA and K is the dose deposition kernel (DDK). The DDK is a 3D spatial distribution of the energy deposited by electrons and positrons, which describes the energy spread from the site of a primary photon interaction [27]. A DDK modeled by Ahnesjö [27] was used in this study, and it is defined by:

$$K(l, \theta) = \frac{A_\theta e^{-a_\theta l} + B_\theta e^{-b_\theta l}}{l^2}, \tag{2}$$

where A_θ, a_θ, B_θ, and b_θ are the parameters of the scattering angle θ, and l is the distance between the interaction site and the dose deposition site. The first term in the numerator of Eq. (2) mainly

Virtual point source

X-ray source

Isocenter

Planning CT images

Detector plane for planning PDI

Virtual water phantom

*SvSD

**SAD

***SID

*SvSD: source to virtual source distance
**SAD: source to axis distance
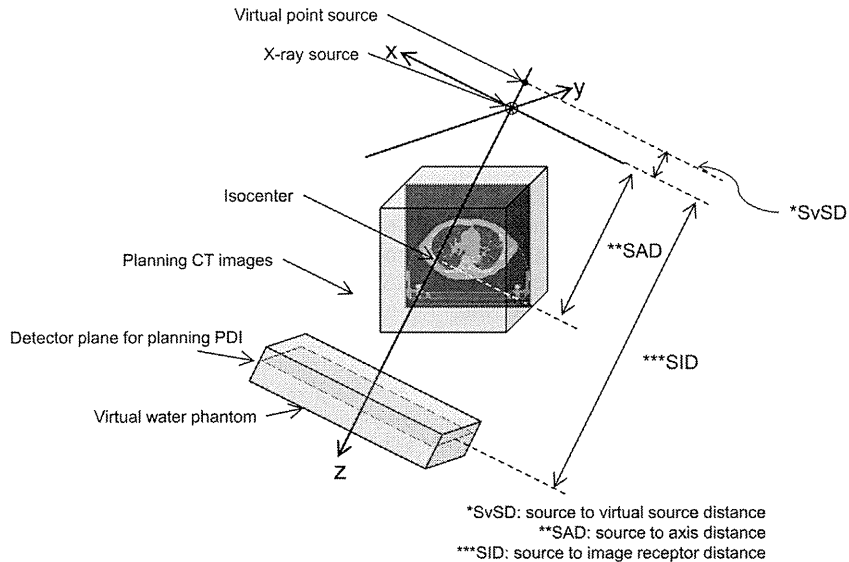***SID: source to image receptor distance

Fig. 4. An illustration of a geometry used for the production of the planning PDI from the planning CT images.

Algorithm 2
An algorithm for the production of the planning PDI.

1.	**INPUT** I^p: planning CT image, K: dose deposition kernel,
2.	res: resolution of planning CT image;
3.	**COMMENTS** $I^{p'}$: isotropic planning CT image, $\mathbf{r}$: position vector,
4.	vwp: virtual waterphantom, voi: VOI,
5.	ρ_{re}: relative electron density to water,
6.	$\mathbf{r}_i$: ith sampling position vector, $d\mathbf{r}$: sampling interval on a ray,
7.	T: TERMA, $\mathbf{r}_0$: the initial position vector of the X-ray source,
8.	ψ: X-ray energy fluence (MeV m^{-2}), E: X-ray energy (MeV),
9.	μ_w: linear attenuation coefficient of water (m^{-1}),
10.	$(\mu/\rho)_w$: mass attenuation coefficient of water (m^2 kg^{-1});
11.	**INITIALIZATION** $vwp \leftarrow 0$;
12.	//**Isotropic Planning CT image by cubic interpolation** [21]
13.	**FOR ALL r DO**
14.	$I^{p'}(\mathbf{r}) \leftarrow$ Cubic interpolation ($I^p(\mathbf{r})$, res);
15.	//**Deamination of VOI** [22]
16.	$voi(\mathbf{r}) \leftarrow$ Cropping VOI ($I^{p'}(\mathbf{r})$, $vwp(\mathbf{r})$);
17.	//**Conversion of the CT value into the electron density** [23]
18.	**IF** $voi(\mathbf{r}) \neq 0$ **THEN**
19.	$\rho_{re}(\mathbf{r}) \leftarrow$ CT to ED conversion ($I^{p'}(\mathbf{r})$, $vwp(\mathbf{r})$);
20.	//**Calculation of WEPL** [24,25]
21.	$W(\mathbf{r}) \leftarrow \sum\limits_{i=0}^{S-1} \rho_{re}(\mathbf{r}_i) \cdot d\mathbf{r}$;
22.	$T(\mathbf{r}) \leftarrow \left(\frac{\mathbf{r}_0}{\mathbf{r}}\right)^2 \int \psi(E, \mathbf{r}_0) \exp(-\mu_w(E) \cdot W(\mathbf{r} - \mathbf{r}_0)) \cdot \left(\frac{\mu}{\rho}\right)_w (E, \mathbf{r}) dE$;
23.	//**Calculation of dose distribution**
24.	$D(\mathbf{r}) \leftarrow T(\mathbf{r}) \cdot K(\mathbf{r})$;
25.	//**Extraction of 2D dose distribution in detector plane**
26.	**IF** $\mathbf{r} \in$ detector plane **THEN**
27.	$\Phi(\mathbf{r}) \leftarrow D(\mathbf{r})$;
28.	**END IF**
29.	**END IF**
30.	**END FOR**
31.	**OUTPUT** Φ: planning PDI;

Algorithm 3
An overall algorithm for the estimation of the simulated 4D "treatment" CT images by using a PDI-based 2D/3D registration between a 2D portal dynamic image and 3D planning CT image.

1.	**INPUT** I^p, I^c, K, res;
2.	**COMMENTS** $\mathbf{s} = [\theta_x, \theta_y, \theta_z, \tau_x, \tau_y, \tau_z, \mu_x, \mu_y, \mu_z]^T$: transformation parameter set,
3.	$\mathbf{s}_{opt}$: optimal transformation parameter set,
4.	**TM**: affine transformation matrix, I^t: deformed planning CT image,
5.	gp: gamma pass rate (3 mm/3%),
6.	I_n: simulated "treatment" CT image in nth frame,
7.	N: max. no. of frames;
8.	**WHILE** $n \leq N$ **DO**
9.	**INITIALIZATION** $\mathbf{s} \leftarrow [0,0,0,0,0,0,1,1,1]^T$
10.	//**Deformation of the planning CT image**
11.	**TM(s)** $\leftarrow$ Affine matrix conversion (**s**);
12.	$I^t(\mathbf{s}) \leftarrow$ **TM(s)** $\cdot I^p$;
13.	//**Production of planning PDI**
14.	$\Phi(\mathbf{s}) \leftarrow$ Planning PDI ($I^t(\mathbf{s})$, K, res);
15.	//**Gamma pass rate as a criteria**
16.	$gp \leftarrow$ Gamma evaluation ($\Phi(\mathbf{s})$, I^c);
17.	**IF** $gp > 98.0$ **THEN**
18.	$\mathbf{s}_{opt} \leftarrow \mathbf{s}$;
19.	**ELSE THEN**
20.	$\mathbf{s}_{opt} \leftarrow$ Optimization of a parameter set of an affine transformation matrix using an LM algorithm (**s**, $\Phi(\mathbf{s})$, I^c, gp); //**Algorithm 4**
21.	**END IF**
22.	$I_n \leftarrow I^t(\mathbf{s}_{opt})$;
23.	**END WHILE**
24.	**OUTPUT** $I = \{I_1, I_2, \ldots I_N\}$: simulated 4D "treatment" CT image;

Table 2
The ranges for the rotation, translation and scaling parameters in the affine transformation.

	Rotation (degrees)	Translation (mm)	Scaling factor
Upper limit	+5	+10	1.09
Lower limit	−5	−10	0.91

describes the energy deposited as a primary dose, and the second term mainly describes the energy deposited as a scattered dose. A 2D dose distribution on the detector plane in the virtual water phantom was estimated as a planning PDI. The detector plane was set at the same position as the EPID on a central beam axis (z-axis).

2.5. Estimation of the simulated 4D "treatment" CT images by using a PDI-based 2D/3D registration

Fig. 5 shows a processing pipeline for estimating the simulated 4D "treatment" CT images based on a PDI-based 2D/3D registration. The simulated 4D "treatment" CT image was estimated by deforming the 3D planning CT image with an affine transformation matrix, which is described in Appendix A.

Algorithm 3 shows an overall algorithm for the estimation of the simulated 4D "treatment" CT images by using a PDI-based 2D/3D registration between a 2D portal dynamic image and 3D planning CT image.

A gamma pass rate (3 mm/3%) between the planning PDI and the dynamic clinical PDI was calculated as a criterion for estimating the "treatment" CT image. The gamma evaluation is an analytical method, which can evaluate the agreement between two dose distributions based on the distance between compared points and the dose difference [29,30]. Fig. 6 shows a schematic representation of the theoretical concept of the gamma evaluation method. The gamma value is defined by:

$$\gamma(\mathbf{r}_c) = \min\{\Gamma_{(\mathbf{r}_r, \mathbf{r}_c)}\} \forall \{\mathbf{r}_r\}, \tag{3}$$

where

$$\Gamma_{(\mathbf{r}_r, \mathbf{r}_c)} = \sqrt{\frac{r^2(\mathbf{r}_r, \mathbf{r}_c)}{\Delta d_M^2} + \frac{\delta^2(\mathbf{r}_r, \mathbf{r}_c)}{\Delta D_M^2}}, \tag{4}$$

$\mathbf{r}_r$ is the reference point, $\mathbf{r}_c$ is the compared point, $r(\mathbf{r}_r, \mathbf{r}_c)$ is the distance between the reference and the compared point, $\delta(\mathbf{r}_r, \mathbf{r}_c)$ is the difference between the dose on the $\mathbf{r}_r$ and $\mathbf{r}_c$, Δd_M is the distance criterion and ΔD_M is the dose difference criterion. The agreement and disagreement criteria become:

$$\gamma(\mathbf{r}_c) \leq 1, \quad \text{agreement},$$

and

$$\gamma(\mathbf{r}_c) > 1, \quad \text{disagreement}. \tag{5}$$

The gamma pass rate is defined by the following equation:

$$\text{Gamma pass rate}(\%) = \frac{\text{No. of agreement points}}{\text{No. of all points}} \cdot 100. \tag{6}$$

If the pass rate exceeded 98.0%, the deformed planning CT image and planning PDI were regarded as the "treatment" CT image and "treatment" PDI, respectively. Otherwise, a transformation parameter set was optimized by using the Levenberg–Marquardt (LM) algorithm [31,32], whose details are explained Appendix B. It should be noted that each parameter range was limited to avoid the use of unlikely large parameters, which may be calculated using the LM algorithm. Table 2 shows the ranges for the rotation, translation and scaling parameters in the affine transformation. If any of the parameters exceeded its range, the upper or lower limit value was used as the parameter. This procedure was applied to all frames of
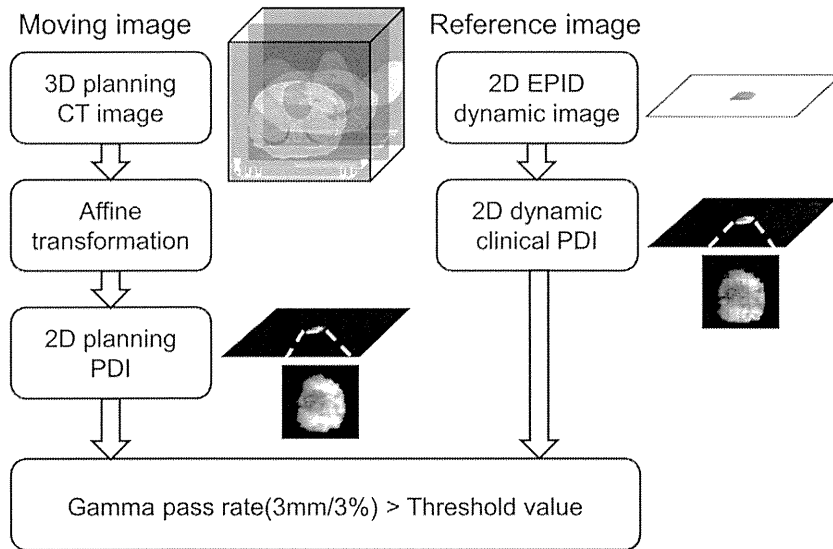
Fig. 5. A processing pipeline for estimating the simulated 4D "treatment" CT images based on a PDI-based 2D/3D registration.
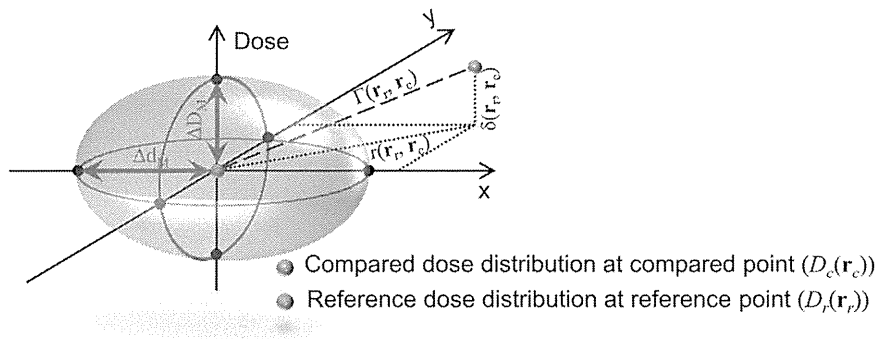

○ Compared dose distribution at compared point ($D_c(\mathbf{r}_c)$)
○ Reference dose distribution at reference point ($D_r(\mathbf{r}_r)$)

Fig. 6. A schematic representation of the theoretical concept of the gamma evaluation method.

Simulated 4D "treatment" CT image   4D dose distribution
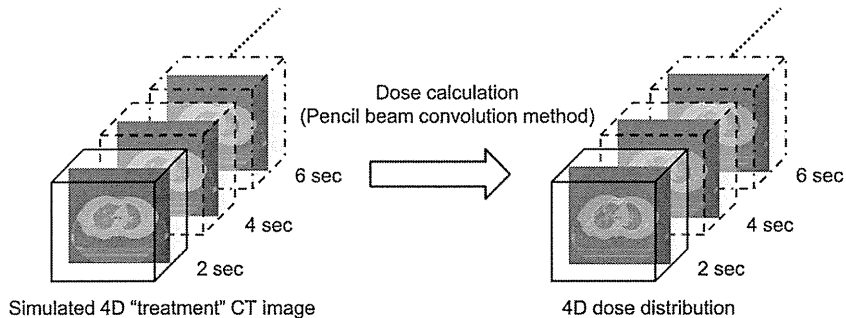
Fig. 7. An illustration of the estimation of the 4D dose distributions.

the EPID dynamic images to estimate the simulated 4D "treatment" CT image.

2.6. Estimation of 4D dose distributions during treatment delivery

Fig. 7 shows an illustration of an estimation of the 4D dose distributions. The 4D dose distributions during the treatment delivery were calculated by applying the PBC algorithm to the simulated 4D "treatment" CT images.

2.7. Evaluation of the proposed framework

The gamma evaluation mentioned above was used to evaluate the proposed framework with respect to the dose distribution similarity between the "treatment" PDI derived from simulated 4D "treatment" CT image and the dynamic clinical PDI derived from the EPID dynamic image. Gamma images, whose pixel value was a γ value, were calculated to visually verify the dose distribution similarity.

In addition, a percentage error between a prescribed dose and an estimated dose at an isocenter was also calculated to evaluate of the proposed framework. The percentage dose error was defined by the following equation:

$$\text{Dose error}(\%) = \frac{|\text{estimated dose} - \text{prescribed dose}|}{\text{prescribed dose}} \cdot 100. \quad (7)$$

Table 3
The mean ± SD of the pass rates between the dynamic clinical PDIs and initial "treatment" PDIs, and those between the dynamic clinical PDIs and "treatment" PDIs.

Case no.	Dynamic clinical PDI vs. initial "treatment" PDI (%)	Dynamic clinical PDI vs. "treatment" PDI (%)	P value
1	98.06 ± 1.03	98.75 ± 0.45	<0.05
2	98.33 ± 1.43	98.47 ± 1.23	>0.05
3	97.30 ± 1.29	99.28 ± 0.44	<0.05
4	98.03 ± 1.44	98.78 ± 1.00	<0.05
5	89.08 ± 2.12	99.32 ± 0.32	<0.05
6	83.67 ± 6.01	90.98 ± 5.25	<0.05
7	74.13 ± 6.81	90.48 ± 5.00	<0.05
8	61.66 ± 4.11	75.53 ± 3.75	<0.05
9	96.32 ± 2.63	97.44 ± 1.68	<0.05
10	96.14 ± 0.73	97.06 ± 1.00	<0.05
Mean	89.27 ± 3.44	94.61 ± 2.71	<0.05

Table 4
The prescribed doses at isocenters, the mean ± SD of the estimated doses for all frames at isocenters and percentage errors for all cases.

Case no.	Prescribed dose at an isocenter (Gy)	Estimated dose at an isocenter (Gy)	Dose error (%)
1	1.50	1.49 ± 0.02	0.67
2	1.71	1.71 ± 0.03	0.00
3	1.50	1.48 ± 0.02	1.33
4	1.54	1.55 ± 0.02	0.65
5	1.50	1.46 ± 0.01	2.67
6	1.70	1.72 ± 0.01	1.18
7	1.50	1.72 ± 0.01	14.67
8	1.50	1.60 ± 0.02	6.67
9	1.50	1.53 ± 0.05	2.00
10	1.51	1.47 ± 0.02	2.65
Mean			3.25 ± 4.43

3. Results

3.1. Four-dimensional dose distributions during treatment time

Fig. 8 shows the 4D dose distributions on the isocenter planes of axial, sagittal and coronal sections at treatment times of 2, 4, and 6 s during the treatment deliveries at a gantry angle of 45° for Case 6 (a) and at a gantry angle of 270° for Case 7 (b). These results suggest that the 4D dose distributions sequentially change in accordance with the respiratory motion.

3.2. Gamma evaluation

Table 3 shows the mean ± standard deviation (SD) of the gamma pass rates between the dynamic clinical PDIs and initial "treatment" PDIs, and those between the dynamic clinical PDIs and the "treatment" PDIs. The initial "treatment" PDIs are planning PDIs, which were obtained from planning CT images without applying the affine transformation, and "treatment" PDIs are also planning PDIs which were obtained by the optimized transformation parameter set. The mean ± SD of the gamma pass rates between the dynamic clinical PDIs and "treatment" PDIs for ten cases was 94.61 ± 2.71%, which was larger than that (89.27 ± 3.44%) of those between the dynamic clinical PDIs and initial "treatment" PDIs. There was a statistically significant difference in the pass rates between the clinical PDIs versus the initial "treatment" PDIs, and the clinical PDIs versus "treatment" PDIs (P < 0.05).

Fig. 9 shows gamma images for Case 5 between the dynamic clinical PDIs and initial "treatment" PDIs, and those between the dynamic clinical PDIs and "treatment" PDIs. Agreement regions between the dynamic clinical PDIs and "treatment" PDIs seemed to be increased comparison with that of between the dynamic clinical PDIs and initial "treatment" PDIs. Dose distribution similarity could be visually verified by calculation of the gamma images.

3.3. Dose errors between prescribed doses and estimated doses

Table 4 shows the prescribed doses at isocenters, the mean ± SD of estimated doses for all frames at isocenters and the percentage errors for all cases. The mean ± SD of the percentage errors between the prescribed dose and the estimated dose at an isocenter for all cases was 3.25 ± 4.43%. The maximum error for ten cases was 14.67% for Case 7 (prescribed dose: 1.50 Gy, estimated dose: 1.72 Gy), and the minimum error was 0.00% for Case 2 (prescribed dose: 1.71 Gy, estimated dose: 1.71 Gy). This result suggests that the proposed framework can be useful to ensure the quality of the radiation therapy by calculating the dose errors between the

delivered dose during the treatment time and the prescribed dose determined by the treatment planning.

4. Discussion

4.1. Gamma pass rates and dose errors

As shown in Table 3, the pass rate between the dynamic clinical PDIs and "treatment" PDIs reached more than 90% for all but Case 8, whose pass rate was 75.53%. Consequently, the proposed framework could estimate the dose at an isocenter during the treatment time, as shown in Table 4. Therefore, the proposed framework could detect the discrepancies between the prescribed doses in treatment plans and estimated doses during the treatment time.

4.2. LM algorithm

The advantage of using the LM algorithm is that it allows for fast computation of the optimization problems. The disadvantage is that the computation of the LM optimization algorithm may be trapped in a local minimum of the objective function, depending on the setting of the initial search points. However, we assumed that the initial point could be close to the global minimum point for two reasons. First, radiological technologists set patients up on a couch according to the treatment plans. Second, the patient bodies were immobilized by stereotactic body frames to limit respiratory motion in this study. Therefore, the propose framework based on the LM optimization algorithm could reach a global minimum.

4.3. Investigation of criterions for optimization

In this study, the gamma pass rate was adopted as a criterion for the LM optimization. This LM algorithm is referred to as the gamma-pass-based LM algorithm (GP-LM). The reason why we adopted the criterion of the gamma pass rate was to reduce the computation time of the optimization while maintaining the optimization accuracy. In general, however, a L2-norm of the parameter increment is used as a criterion for the LM algorithm [32].

This typical method is referred to as the standard LM algorithm (S-LM) in this paper. Moreover, a normalized mutual information (NMI) was employed as a criterion for the LM algorithm (NMI-based LM algorithm: NMI-LM), because the NMI has been widely utilized for evaluation of the image similarity [33]. We compared the results obtained by the proposed framework based on the GP-LM, S-LM and NMI-LM. Table 5 shows the criterions of GP-LM, S-LM and NMI-LM. The threshold value of the NMI was empirically determined.
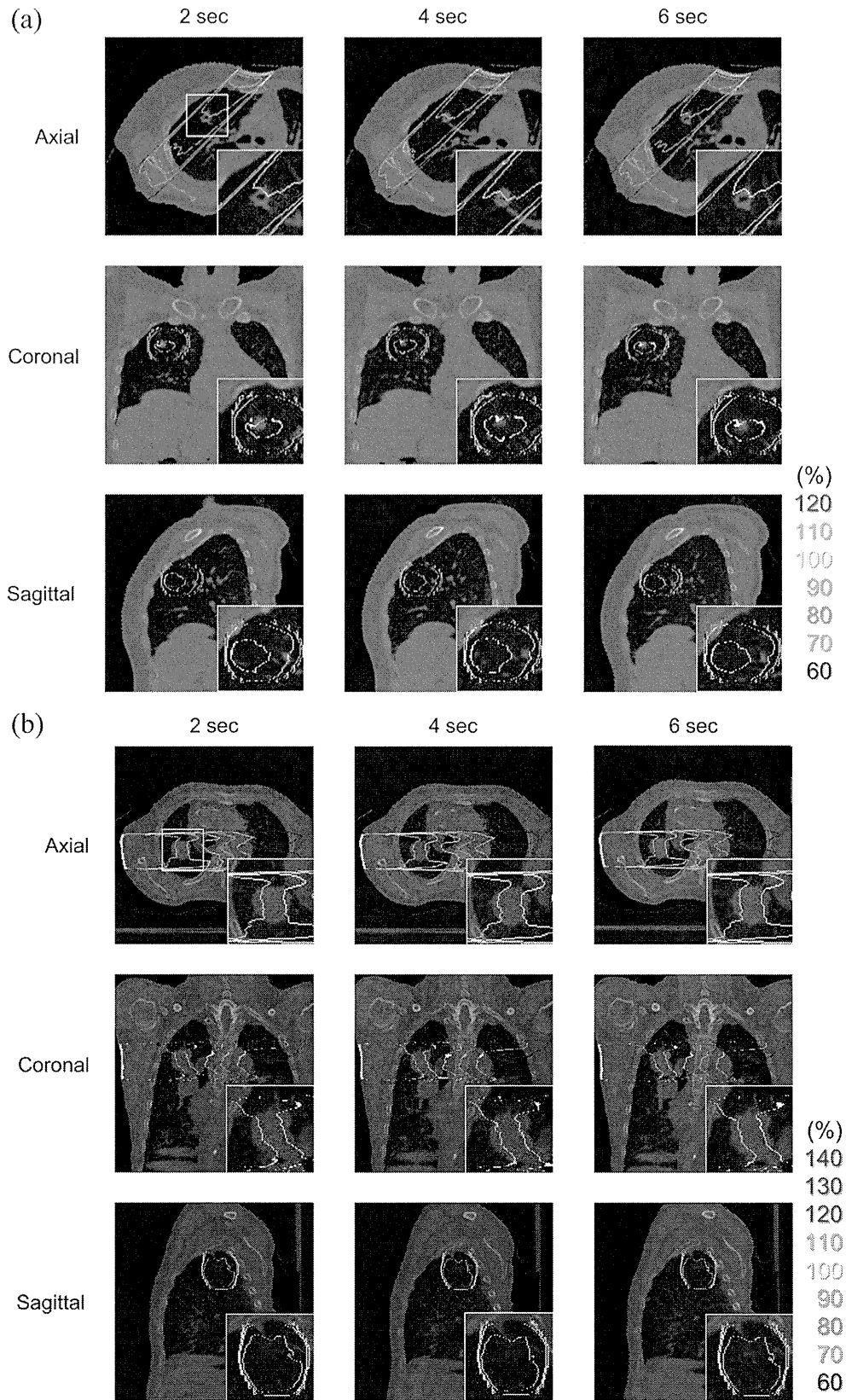
Fig. 8. The four-dimensional dose distributions on the isocenter planes of axial, sagittal and coronal sections at treatment times of 2, 4, and 6 s during treatment deliveries at a gantry angle of 45° for Case 6 (a) and at a gantry angle of 270° for Case 7 (b). Inserts depict enlarged images around isocenters.
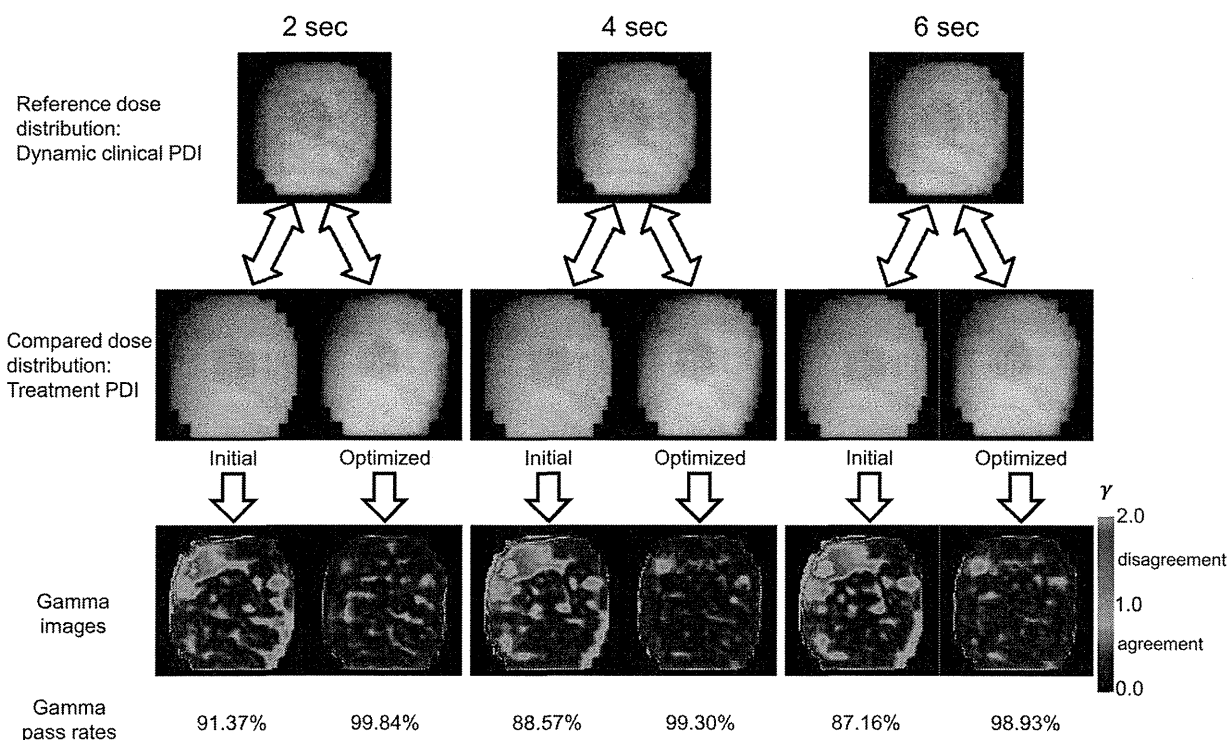
Fig. 9. Gamma images for Case 5 between the dynamic clinical PDIs and initial "treatment" PDIs, and those between the dynamic clinical PDIs and "treatment" PDIs.

Table 5
The criterions of the gamma-pass-based Levenberg–Marquardt (LM), standard LM and normalized mutual information (NMI)-based LM algorithms.

LM	Criterion
Gamma-pass-based LM	$gp > 98.0$
Standard LM	$||\Delta s|| < 1.0 \times 10^{-3}$ [34]
NMI-based LM	$NMI > 1.2$

Table 6
The mean ± SD of the gamma pass rates at treatment times of 2, 4, and 6 s during treatment deliveries between the dynamic clinical PDIs and the "treatment" PDIs using the gamma-pass-based Levenberg–Marquardt (LM), standard LM and normalized mutual information (NMI)-based LM algorithms.

Case no.	Gamma-pass-based LM (%)	Standard LM (%)	NMI-based LM (%)
1	98.89 ± 0.44	98.69 ± 0.51	99.26 ± 0.79
2	98.81 ± 1.27	98.59 ± 1.15	89.50 ± 3.24
3	99.41 ± 0.19	99.61 ± 0.15	98.65 ± 0.55
4	98.94 ± 0.53	99.95 ± 0.07	98.74 ± 0.50
5	99.36 ± 0.46	99.77 ± 0.16	99.06 ± 0.21
6	91.94 ± 7.03	91.64 ± 6.77	88.11 ± 4.58
7	81.70 ± 7.95	81.12 ± 7.79	81.57 ± 8.24
8	74.66 ± 2.12	77.03 ± 6.58	57.38 ± 4.89
9	97.29 ± 2.00	98.59 ± 1.15	96.35 ± 5.51
10	96.63 ± 1.40	96.41 ± 1.44	93.82 ± 1.20
Mean	93.76 ± 3.54	94.14 ± 3.94	90.24 ± 3.95

Table 7
The mean calculation times for three EPID frames at treatment times of 2, 4, and 6 s for all cases using the gamma-pass-based Levenberg–Marquardt (LM), standard LM and normalized mutual information (NMI)-based LM algorithms.

Case no.	Gamma-pass-based LM (min)	Standard LM (min)	NMI-based LM (min)
1	39.7	504.7	116.0
2	45.7	137.7	113.1
3	99.0	200.0	160.6
4	27.3	133.7	213.8
5	59.3	369.3	80.7
6	315.7	291.3	94.2
7	269.7	202.3	317.1
8	314.0	682.3	280.3
9	162.0	197.3	217.9
10	269.3	189.0	110.4
Mean	160.2	290.8	170.4

Table 6 shows the mean ± SD of the gamma pass rates at treatment times of 2, 4, and 6 s during treatment deliveries between the dynamic clinical PDIs and the "treatment" PDIs using the GP-LM, S-LM and NMI-LM. The mean ± SD of the pass rates between the dynamic clinical PDIs and "treatment" PDIs based on the S-LM for the ten cases was 94.14 ± 3.94%, which was slightly larger than the other pass rates (GP-LM: 93.76 ± 3.54%, NMI-LM: 90.24 ± 3.95%) between the dynamic clinical PDIs and "treatment" PDIs. There was not a statistically significant difference in the pass rates between the dynamic clinical PDIs versus "treatment" PDIs based on the S-LM compared to that based on the GP-LM ($P > 0.05$). On the other hand, the pass rates obtained by the GP-LM were significantly larger than those by the NMI-LM ($P < 0.05$). Therefore, the proposed framework based on the GP-LM appears to have the same optimization accuracy as that based on the S-LM, but it was superior to that based on the NMI-LM.

Moreover, the computation times were compared between the three frameworks. Table 7 shows the means of the calculation times for three EPID frames at treatment times of 2, 4, and 6 s for all cases using the GP-LM, S-LM and NMI-LM. The mean calculation times for all cases based on the GP-LM, S-LM and NMI-LM were 160.2 min, 290.8 min and 170.4 min, respectively. Therefore, the proposed framework based on the GP-LM was faster than the other two methods. However, there was not a statistically significant difference in the computational times between the GP-LM and NMI-LM ($P > 0.05$).

In summary, the proposed framework based on the GP-LM could be better than the other two methods in terms of the pass rate and computational time.

4.4. Limitations

There are three limitations that may be raised in this study. First, phantom experiments should be performed to evaluate the 4D dose distribution estimated by the proposed framework, because it is very difficult to verify the in vivo dose distribution. Second, the computation time (about 3 h on average) should be reduced using parallel computing methods, such as general-purpose computing on a graphics processing unit (GPGPU), because it took a long time to calculate the 3D dose distributions using the PBC algorithm. Third, non-linear registration techniques should be employed in the PDI-based 2D/3D registration, because physiological organ and/or tumor motions are non-linear.

5. Conclusion

We have developed an automated framework for estimation of the 4D dose distributions in SBRT based on a PDI-based 2D/3D image registration between the EPID dynamic images and planning CT images. The proposed framework appears to be feasible for estimating the 4D dose distributions in patients' bodies during treatment delivery. Moreover, the framework seems to be useful for ensuring the quality of the radiation therapy by calculating the dose errors between the delivered dose during the treatment time and the prescribed dose determined by the treatment planning.

Acknowledgements

Appendix A. Affine transformation matrix employed for deforming 3D planning CT images.

The affine transformation matrix includes a nine-dimensional transformation parameter vector, $s = [\theta_x, \theta_y, \theta_z, \tau_x, \tau_y, \tau_z, \mu_x, \mu_y, \mu_z]^T$, which represents the internal or external patient body motion related to respiration, where θ_x, θ_y, and θ_z are the rotations around the x, y and z axes, respectively, τ_x, τ_y, and τ_z are the translations in x, y and z directions, respectively and μ_x, μ_y, and μ_z are the scaling factors in the x, y and z directions, respectively. Fig. 10 shows the nine affine transformation parameters. The affine transformation matrix, T_{aff} was expressed by:

$$T_{aff} = RS + t, \tag{8}$$

where

$$R = \begin{bmatrix} \cos\theta_y \cos\theta_z & \cos\theta_x \sin\theta_z + \sin\theta_z \sin\theta_y \cos\theta_z & \sin\theta_x \sin\theta_z - \cos\theta_x \sin\theta_y \cos\theta_z & 0 \\ \sin\theta_y & \cos\theta_x \cos\theta_z + \sin\theta_x \sin\theta_y \sin\theta_z & \sin\theta_x \cos\theta_z + \cos\theta_x \sin\theta_y \sin\theta_z & 0 \\ \sin\theta_y & \sin\theta_x \cos\theta_y & \cos\theta_x \cos\theta_y & 0 \\ 0 & 0 & 0 & 1 \end{bmatrix},$$

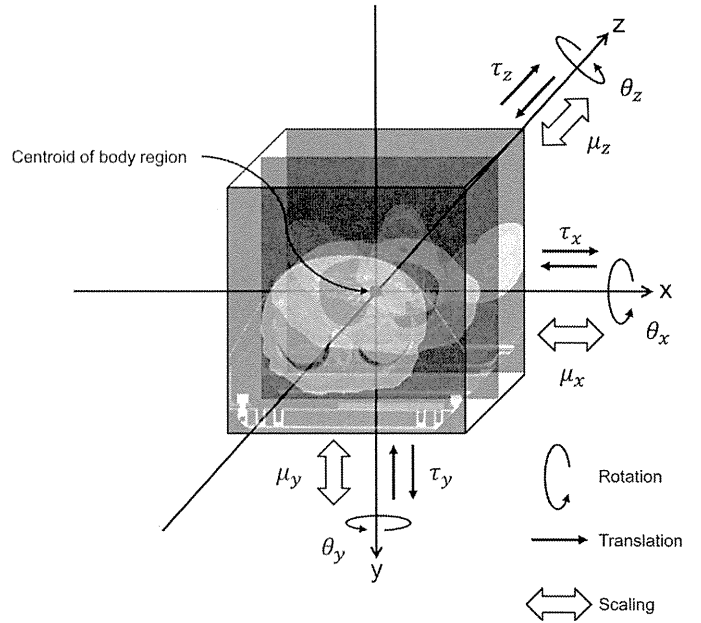$$S = \begin{bmatrix} \mu_x & 0 & 0 & 0 \\ 0 & \mu_y & 0 & 0 \\ 0 & 0 & \mu_z & 0 \\ 0 & 0 & 0 & 1 \end{bmatrix},$$

Fig. 10. The nine affine transformation parameters.

and

$$t = \begin{bmatrix} 0 & 0 & 0 & \tau_x \\ 0 & 0 & 0 & \tau_y \\ 0 & 0 & 0 & \tau_z \\ 0 & 0 & 0 & 0 \end{bmatrix}. \tag{9}$$

Here, R, S and t are the rotation, scaling and translation matrices, respectively.

Appendix B. Optimization of an affine transformation parameter set based on a LM algorithm.

The LM algorithm is a standard optimization technique used to solve non-linear least squares problems. In addition, the LM algorithm is one of gradient-based optimization techniques, which combines a Gauss–Newton method with a steepest descent method [31,32].

Algorithm 4 shows an overall algorithm of optimization of a parameter set of an affine transformation matrix using an LM algorithm. A new parameter set, s' was calculated by:

$$s' = s + \Delta s, \tag{10}$$

where s is a previous parameter set and Δs is a parameter increment. The parameter increment, Δs was calculated by:

$$\Delta s = (H_s + cD[H_s]^{-1}) \cdot (-\nabla_s J), \tag{11}$$

where H_s is the Hessian matrix, $\nabla_s J$ is the gradient of the objective function, $D[H_s]$ is the diagonal matrix of the Hessian matrix and c is the damping factor, whose initial value was 0.0001 [35]. If $H_s + cD[H_s]$ has become a singular matrix, the iterative optimization has been stopped and the transformation parameter set with

Algorithm 4
An overall algorithm of optimization of a parameter set of an affine transformation matrix using an LM algorithm.

---

1. **INPUT s,** $\Phi(\mathbf{s})$, I^c, gp;
2. **COMMENTS** J: objective function, (i,j): pixel coordinate,
3. $\nabla_\mathbf{s}J$: gradient of the objective function, $\mathbf{H_s}$: Hessian matrix,
4. c: damping parameter, $\mathbf{D[H_s]}$: diagonal matrix of Hessian matrix,
5. $\Delta\mathbf{s}$: parameter increment, $\mathbf{s}'$: new transformation parameter vector,
6. J': new objective function, *coarse*: no. of coarse searching,
7. *fine*: no. of fine searching;
8. **INITIALIZATION** $gp_{max} \leftarrow gp$, $\mathbf{s}_{gpmax} \leftarrow \mathbf{s}$, $c \leftarrow 0.0001$, *coarse* $\leftarrow 0$,
9. *fine* $\leftarrow 0$;
10. //**Calculation of an objective function**
11. $J \leftarrow \frac{1}{2}\sum_{i,j}\{\Phi(\mathbf{s})_{i,j} - I^c_{i,j}\}^2$;
12. **LOOP1** //**Coarse searching**
13. //**Calculation of a gradient of the objective function and Hessian matrix**
14. $\nabla_\mathbf{s}J \leftarrow \sum_{i,j}\{\Phi(\mathbf{s})_{i,j} - I^c_{i,j}\}\cdot\{\nabla_\mathbf{s}\Phi(\mathbf{s})_{i,j}\}$;
15. $\mathbf{H_s} \leftarrow \sum_{i,j}\{\nabla_\mathbf{s}\Phi(\mathbf{s})_{i,j}\}\cdot\{\nabla_\mathbf{s}\Phi(\mathbf{s})_{i,j}\}^T$;
16. **LOOP2** //**Fine searching**
17. //**Calculation of the new transformation parameter set**
18. **IF** $det(\mathbf{H_s} + c\mathbf{D[H_s]}) = 0.0$ **THEN**
19. $\quad$ $\mathbf{s}_{opt} \leftarrow \mathbf{s}_{gpmax}$;
20. $\quad$ **GO TO 46 line**
21. **END IF**
22. $\Delta\mathbf{s} \rightarrow (\mathbf{H_s} + c\mathbf{D[H_s]})^{-1}\cdot(-\nabla_\mathbf{s}J)$;
23. $\mathbf{s}' \leftarrow \mathbf{s} + \Delta\mathbf{s}$;
24. //**Calculation of the new objective function and gamma pass rate**
25. $gp \leftarrow$ Gamma evaluation $(\Phi(\mathbf{s}'), I^c)$;
26. $J' \leftarrow \frac{1}{2}\sum_{i,j}\{\Phi(\mathbf{s}')_{i,j} - I^c_{i,j}\}^2$;
27. **IF** $gp > gp_{max}$ **THEN**
28. $\quad$ $gp_{max} \leftarrow gp$, $\mathbf{s}_{gpmax} \leftarrow \mathbf{s}'$;
29. **END IF**
30. //**Judgment**
31. **IF** $gp > 98.0$ **THEN**
32. $\quad$ $\mathbf{s}_{opt} \leftarrow \mathbf{s}'$;
33. **ELSE IF** *coarse* $= 5$ **OR** *fine* $= 10$ **THEN**
34. $\quad$ $\mathbf{s}_{opt} \leftarrow \mathbf{s}_{gpmax}$;
35. **ELSE IF** $J > J'$ **THEN**
36. $\quad$ $\mathbf{s} \leftarrow \mathbf{s}'$, $c \leftarrow \frac{c}{10}$;
37. $\quad$ *coarse*++, *fine* $\leftarrow 0$;
38. $\quad$ **GO TO LOOP1**
39. **ELSE THEN**
40. $\quad$ $c \leftarrow 10c$;
41. $\quad$ *fine*++;
42. $\quad$ **GO TO LOOP2**
43. **END IF**
44. **END IF**
45. **END IF**
46. **OUTPUT** $\mathbf{s}_{opt}$: optimal transformation parameter set;

---

the largest pass rate in an entire iteration was regarded as the optimal transformation parameter set. An objective function, J, gradient, $\nabla_\mathbf{s}J$, and Hessian matrix, $\mathbf{H_s}$ were calculated by the following equations:

$$J = \frac{1}{2}\sum_{i,j}\{\Phi(\mathbf{s})_{i,j} - I^c_{i,j}\}^2, \tag{12}$$

$$\nabla_\mathbf{s}J = \sum_{i,j}\{\Phi(\mathbf{s})_{i,j} - I^c_{i,j}\}\cdot\{\nabla_\mathbf{s}\{\Phi(\mathbf{s})_{i,j} - I^c_{i,j}\}\}$$

$$= \sum_{i,j}\{\Phi(\mathbf{s})_{i,j} - I^c_{i,j}\}\cdot\{\nabla_\mathbf{s}\Phi(\mathbf{s})_{i,j}\}, \tag{13}$$

and

$$\mathbf{H_s} = \sum_{i,j}\begin{pmatrix} \dfrac{\partial^2\Phi(\mathbf{s})_{i,j}}{\partial\theta_x^2} & \cdots & \dfrac{\partial^2\Phi(\mathbf{s})_{i,j}}{\partial\theta_x\partial\mu_z} \\ \vdots & \ddots & \vdots \\ \dfrac{\partial^2\Phi(\mathbf{s})_{i,j}}{\partial\mu_z\partial\theta_x} & \cdots & \dfrac{\partial^2\Phi(\mathbf{s})_{i,j}}{\partial\mu_z^2} \end{pmatrix}$$

$$\approx \sum_{i,j}\{\nabla_\mathbf{s}\Phi(\mathbf{s})_{i,j}\}\cdot\{\nabla_\mathbf{s}\Phi(\mathbf{s})_{i,j}\}^T, \tag{14}$$

where i and j are the pixel coordinates, $\Phi(\mathbf{s})$ is the planning PDI calculated from deformed planning CT images using $\mathbf{s}$, I^c is the dynamic clinical PDI and $\nabla_\mathbf{s}\Phi(\mathbf{s}) = \left[\frac{\partial\Phi(\mathbf{s})_{i,j}}{\partial\theta_x}, \frac{\partial\Phi(\mathbf{s})_{i,j}}{\partial\theta_y}, \frac{\partial\Phi(\mathbf{s})_{i,j}}{\partial\theta_z}, \frac{\partial\Phi(\mathbf{s})_{i,j}}{\partial\tau_x}, \frac{\partial\Phi(\mathbf{s})_{i,j}}{\partial\tau_y}, \frac{\partial\Phi(\mathbf{s})_{i,j}}{\partial\tau_z}, \frac{\partial\Phi(\mathbf{s})_{i,j}}{\partial\mu_x}, \frac{\partial\Phi(\mathbf{s})_{i,j}}{\partial\mu_y}, \frac{\partial\Phi(\mathbf{s})_{i,j}}{\partial\mu_z}\right]^T$ is the gradient vector of the planning PDI. The first derivative was approximated by a finite difference [36] as follows:

$$\frac{\partial\Phi(\mathbf{s})_{i,j}}{\partial\tau_x} \approx \frac{\Phi(\mathbf{s} + \Delta\mathbf{s}_{\tau_x})_{i,j} - \Phi(\mathbf{s})_{i,j}}{\Delta\tau_x}, \tag{15}$$

where $\Delta\mathbf{s}_{\tau_x} = [0, 0, 0, \Delta\tau_x, 0, 0, 0, 0, 0]^T$. The $\Phi(\mathbf{s} + \Delta\mathbf{s}_{\tau_x})$ is obtained from the planning PDI by changing the translation τ_x to $\tau_x + \Delta\tau_x$, while keeping the other parameters fixed. This calculation was applied to all elements of the transformation parameter set. A new objective function, J', and the gamma pass rate, gp were calculated by using the $\mathbf{s}'$. If the gp exceeded 98.0%, the optimization was finished, and the new parameter set, $\mathbf{s}'$ was regarded as an optimal solution. If the gp did not exceeded 98.0%, the algorithm proceeded to the next step of evaluation of the objective function. If the J' was smaller than the J, the parameters of c, J' and $\mathbf{s}'$ were updated to $c/10$, J and $\mathbf{s}$, and the procedure returned to the calculation of the gradient and Hessian matrix. This process was called coarse searching. If the J' was not smaller than the J, the c was updated to $10c$, and the procedure returned to the step of calculating the $\Delta\mathbf{s}$. This process was denoted as fine searching. The maximum number of coarse searching iterations and that of fine searching iterations were 5 and 10 times respectively. If the procedure was iterated until the maximum numbers, the iterative optimization has been stopped and the transformation parameter set with the largest pass rate in an entire iteration was regarded as the optimal transformation parameter set.

References

[1] Benedict SH, Yenice KM, Folllowill D, Galvin JM, Hinson W, Kavanagh B, et al. Stereotactic body radiation therapy: the report of AAPM Task Group 101. Med Phys 2010;37(8):4078–101.

[2] Kupelian PA, Potters L, Khuntia D, Ciezki JP, Reddy CA, Reuther AM, et al. Radical prostatectomy, external beam radiotherapy <72 Gy, external beam radiotherapy > or =72 Gy, permanent seed implantation, or combined seeds/external beam radiotherapy for stage T1–T2 prostate cancer. Int J Radiat Oncol Biol Phys 2004;58(1):25–33.

[3] Vassil AD, Murphy ES, Reddy CA, Angermeier KW, Altman A, Chehade N, et al. Five year biochemical recurrence free survival for intermediate risk prostate cancer after radical prostatectomy, external beam radiation therapy or permanent seed implantation. Urology 2010;76(5):1138–42.

[4] Onishi H, Shirato H, Nagata Y, Hiraoka M, Fujino M, Gomi K, et al. Stereotactic body radiotherapy (SBRT) for operable stage I non-small-cell lung cancer: can SBRT be comparable to surgery? Int J Radiat Oncol Biol Phys 2011;81(5):1352–8.

[5] Bortfeld T, Jiang SB, Rietzel E. Effects of motion on the total dose distribution. Semin Radiat Oncol 2004;14(1):41–51.

[6] Rosu M, Balter JM, Chetty IJ, Kessler ML, McShan DL, Balter P, et al. How extensive of a 4D dataset is needed to estimate cumulative dose distribution plan evaluation metrics in conformal lung therapy? Med Phys 2007;34(1):233–45.

[7] McNutt TR, Mackie TR, Reckwerdt P, Paliwal BR. Modeling dose distributions from portal dose images using the convolution/superposition method. Med Phys 1996;23(8):1381–92.

357

[8] Partridge M, Ebert M, Hesse BM. IMRT verification by three-dimensional dose reconstruction from portal beam measurements. Med Phys 2002;29(8):1847–58.

[9] Renner WD, Sarfaraz M, Eari MA, Yu CX. A dose delivery verification method for conventional and intensity-modulated radiation therapy using measured field fluence distributions. Med Phys 2003;30(11):2996–3005.

[10] Steciw S, Warkentin B, Rathee S, Fallone BG. Three-dimensional IMRT verification with a flat-panel EPID. Med Phys 2005;32(2):600–12.

[11] van Elmpt WJ, Nijsten SM, Schiffeleers RF, Dekker AL, Mijnheer BJ, Lambin P, et al. A Monte Carlo based three-dimensional dose reconstruction method derived from portal dose images. Med Phys 2006;33(7):2426–34.

[12] Keall P. 4-dimensional computed tomography imaging and treatment planning. Semin Radiat Oncol 2004;14(1):81–90.

[13] Flampouri S, Jiang SB, Sharp GC, Wolfgang J, Patel AA, Choi NC. Estimation of the delivered patient dose in lung IMRT treatment based on deformable registration of 4D-CT data and Monte Carlo simulations. Phys Med Biol 2006;51(11):2763–79.

[14] Guckenberger M, Wilbert J, Krieger T, Richter A, Baier K, Meyer J, et al. Four-dimensional treatment planning for stereotactic body radiotherapy. Int J Radiat Oncol Biol Phys 2007;69(1):276–85.

[15] Admiraal MA, Schuring D, Hurkmans CW. Dose calculations accounting for breathing motion in stereotactic lung radiotherapy based on 4D-CT and the internal target volume. Radiother Oncol 2008;86(1):55–60.

[16] Gendrin C, Furtado H, Weber C, Bloch C, Figl M, Pawiro SA, et al. Monitoring tumor motion by real time 2D/3D registration during radiotherapy. Radiother Oncol 2012;102(2):274–80.

[17] Chen J, Chuang CF, Morin O, Aubin M, Pouliot J. Calibration of an amorphous-silicon flat panel portal imager for exit-beam dosimetry. Med Phys 2006;33(3):584–94.

[18] Mizoguchi A, Arimura H, Shioyama Y, Nakamoto T, Yoshidome S, Hirose T, et al. Estimation of four-dimensional dose distribution using electronic portal imaging device in radiation therapy. IEICE Trans D 2013;J96–D(4):813–23 (Japanese edition).

[19] Sham E, Seuntjens J, Devic S, Podgorsak EB. Influence of focal spot on characteristics of very small diameter radiosurgical beams. Med Phys 2008;35(7):3317–30.

[20] Anai S, Arimura H, Nakamura K, Araki F, Matsuki T, Yoshikawa H, et al. Estimation of focal and extra-focal radiation profiles based on Gaussian modeling in medical linear accelerators. Radiol Phys Technol 2011;4(2):173–9.

[21] Keys RG. Cubic convolution interpolation for digital image processing. IEEE Trans Acoust 1981;29(6):1153–60.

[22] Arimura H, Itano W, Shioyama Y, Matsushita N, Magome T, Yoshitake T, et al. Computerized estimation of patient setup errors in portal images based on localized pelvic templates for prostate cancer radiotherapy. J Radiat Res 2012;53(6):961–72.

[23] Saw CB, Loper A, Komanduri K, Combine T, Huq S, Scicutella C. Determination of CT-to-density conversion relationship for image-based treatment planning systems. Med Dosim 2005;30(3):145–8.

[24] Seco J, Evans PM. Assessing the effect of electron density in photon dose calculations. Med Phys 2006;33(2):540–52.

[25] Yang M, Virshup G, Mohan R, Shaw CC, Zhu XR, Dong L. Improving accuracy of electron density measurement in the presence of metallic implants using orthovoltage computed tomography. Med Phys 2008;35(5):1932–41.

[26] Mackie TR, Scrimger JW, Battista JJ. A convolution method of calculating dose for 15-MV X-rays. Med Phys 1985;12(2):188–96.

[27] Ahnesjö A. Collapsed cone convolution of radiant energy for photon dose calculation in heterogeneous media. Med Phys 1989;16(4):577–92.

[28] Battista JJ, Sharpe MB. True three-dimensional dose computations for megavoltage X-ray therapy: a role for the superposition principle. Australas Phys Eng Sci Med 1992;15(4):159–78.

[29] Low DA, Harms WB, Mutic S, Purdy JA. A technique for the quantitative evaluation of dose distributions. Med Phys 1998;25(5):656–61.

[30] Low DA, Dempsey JF. Evaluation of the gamma dose distribution comparison method. Med Phys 2003;30(9):2455–64.

[31] Levenberg K. A method for the solution of certain non-linear problems in least squares. Quart Appl Math 1944;2:164–8.

[32] Marquardt DW. An algorithm for least-squares estimation of nonlinear parameters. J Soc Indust Appl Math 1963;11(2):431–41.

[33] Pluim JP, Maintz JB, Viergever MA. Mutual-information-based registration of medical images: a survey. IEEE Trans Med Imaging 2003;22(8):986–1004.

[34] Press WH, Flannery BP, Teukolsky SA, Vetterling WT. Numerical recipes. Cambridge: Cambridge University Press; 1986.

[35] Nielsen HB. Damping parameter in Marquardt's method. Techcinal report IMM-REP-1999-05; 1999.

[36] Xu L, Wan JW. Real-time intensity-based rigid 2D–3D medical image registration using RapidMind Multi-core Development Platform. In: Conf Proc IEEE Eng Med Biol Soc. vol. 2008. 2008. p. 5382–5.